ILMATIETEEN LAITOS

Universität Zürich

High-Speed Stream Structures and Interaction with the Magnetosphere

MASTER'S THESIS

presented by

Gisela Baumann

carried out under the supervision of

Assoc. Prof. E. Tanskanen, Prof. T. Pulkkinen

at the Finnish Meteorological Institute

Space Research Unit

and

Prof. P. Jetzer

from the Institute of Theoretical Physics

of the University of Zürich

between June 2007 and January 2008

submitted on February 7, 2008

Contents

Abstract

The task for this Master's thesis was to examine periods of large-scale high solar wind speed during the years 1998 – 2007, using the interplanetary observations by the Advanced Composition Explorer (ACE). As a first step an improved definition of large-scale high-speed streams was developed. On this basis the structure of high-speed streams was analyzed, their effects on magnetospheric activity as well as their dependance on the solar cycle and the solar rotation. Furthermore the relation between high solar wind speed and the co-rotating interaction regions was examined.

The high solar wind speed is one driver of space weather. Analysing the solar wind parameters of high-speed streams and their relation to geomagnetic activity will enhance our ability to understand and predict space weather events.

1 Introduction

High-speed streams (HSSs) originating from coronal holes of the Sun have been detected by spacecrafts as increases in the solar wind velocity lasting up to several days. They have multiple effects on the Earth and the interplanetary space. Therefore the analysis of high-speed streams is of high importance for solar and heliospheric research.

It is known that the activity of the Sun is related to the number of sunspots and has a periodicity of 11 years, the solar cycle. During the declining phase of the solar cycle, high-speed solar wind streams occur more frequently than during the increasing phase but high-speed solar ejecta less frequently. HSSs co-rotate with the 27-day rotation period of the Sun. The occurrence of auroral substorms shows the same frequency.

HSSs strongly modulate substorms. High levels of auroral-region activity, represented by the AL index, can be observed during HSSs. This activity has been attributed to the negative B_z component of the interplanetary magnetic field that leads to reconnection and substorms. These then can enable energetic particles to penetrate the magnetosphere and further into the upper atmosphere, where, for instance, they can cause damage to communication systems. By studying HSSs and their relation to substorms, the forecasting of space weather effects can be made easier.

To complement the existing knowledge my first task was to find a good approach to define HSSs and to study their structure in the solar wind parameters and occurrence in short time scales (month) and over several years ($\sim$ solar cycle). To extract statistics on the features of high-speed streams a superposed epoch analysis was conducted. I for instance examined the velocity increase during HSSs, which

was found to be delayed compared to the other solar wind parameters. I aimed at the explanation for such a delay by gaining understanding of the process from where high-speed streams are produced. This is in close connection to how co-rotating interaction regions are related to HSSs, for which a partial answer could be found. Also the interaction of HSSs with the Earth, for instance how they trigger substorms, is not yet fully understood. I show a possible connection between HSSs and substorms and found an unexpected behaviour of the magnetic field fluctuation in relation to the proton density. Further I used a known characteristic of HSS to separate them from coronal mass ejections (CMEs) which will help in the next step of this research. With the data provided by the still operational ACE spacecraft recent research on the behaviour of high-speed solar winds during different phases of the solar cycle could be conduced which is then compared to similar statistics of substorms.

First of all the basic knowledge of this research field is summarised in the introduction, using the source [6] or [9] if nothing else is remarked. Section 2 gives a general idea of the ACE spacecraft and the two most important instruments onboard, from which I used the data. From Section 3 onwards starts the second part, consisting of the own research results. It begins with the definition and its influence on the occurrence of HSSs. Then their relation to the solar cycle and the solar rotation will be discussed. After a short glance at the AL index behaviour during HSSs, the typical HSS features are finally introduced, and how they differ from other structures originating from the Sun. In Section 7 there are some points of the research of this thesis listed that still require some improvement. Section 8 summarises the results and the following Section 9 gives a motivation and an outlook on what will be done in the future in this research field.

1.1 The anatomy of the Sun

The Sun is a vast massive ($3.3 \cdot 10^5$ times the mass of the Earth) ball of gas consisting of hydrogen (90 %) and helium (10 %), which are mostly ionized because of the very high temperature.

The atmosphere of the Sun consists of three layers. The lowest is the photosphere having a thickness of 500 km. This layer emits most of the light of the Sun and has a density of $10^{17}\,\mathrm{cm}^{-3}$. The temperature falls to a minimum value of 4200 K. The next layer further out is the more transparent chromosphere. Its temperature at greater altitudes in the atmosphere increases towards the outermost layer as well as the density. At an altitude of about $2 - 3 \cdot 10^9$ m the solar corona reaches a temperature of $2 \cdot 10^6$ K.

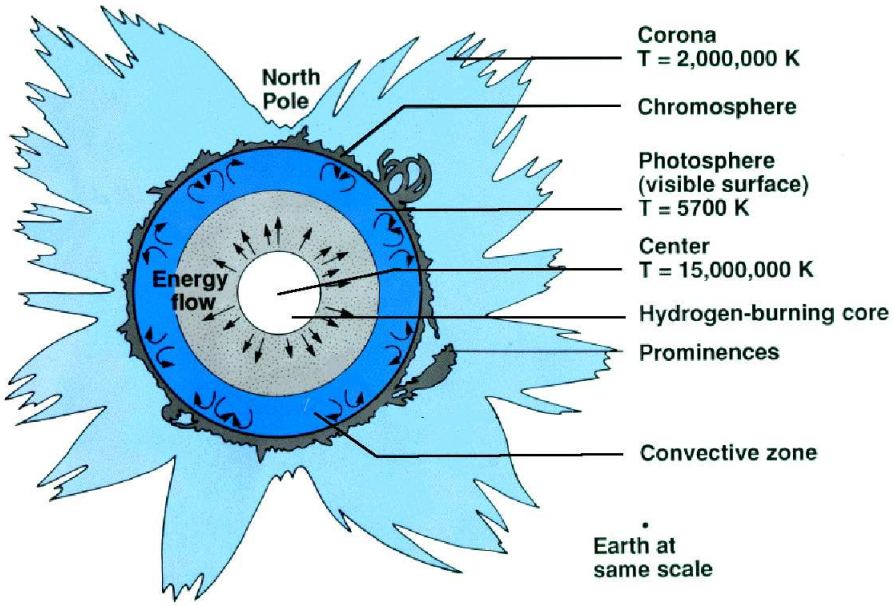

Fig. 1: The anatomy of the Sun, adapted from [29]

The thin surface absorbs most of the energy and radiates it out at a temperature of 5778 K. The pressure of the Sun consists of two components; the gas pressure p_{Gas} and the radiation pressure p_R. The radiation pressure is important only in the solar atmosphere and in the solar wind. The temperature and density gradient in the solar atmosphere leads to a high difference in the gas pressure and thus to an expansion that drives the solar wind.

The energy is produced in the hot central core by nuclear fusion. From the core the energy flows carried by γ-rays in the radiation zone outward to a distance of about 0.72 solar radii, where the radiation loses its efficiency and convective motion takes over the energy transfer [22]. The energy diffusion process in the dense gas of

the radiation zone takes around 170'000 years to reach the convection zone in which zone the medium is so opaque that the energy transport is much faster; it only takes about 10 days to penetrate through it. The convection zone starts where radiation is no longer able to remove all the energy coming from the core. At that point, the gas starts to heat and becomes convectively unstable.

The solar surface rotation speed can be determined by observing the motion of structures, such as sunspots, on the visible surface of the Sun. One solar rotation lasts about 27 days. However, the rotation is not rigid, but the equatorial surface rotates faster than the high-latitude regions. This is known as differential rotation.

The energy coming from the core, the convection zone and the differential rotation finally form the internal dynamo of the Sun, producing the solar magnetic field.

1.1.1 The solar cycle

Table 1: Dates of solar activity minima and maxima since 1960

Cycle number	Date of minima	Date of maxima
20	1964.9	1968.9
21	1976.5	1979.9
22	1986.8	1989.6
23	1996.9	2000.5
24	Jan. 2008	Oct. 2011 or Aug. 2012

The sunspot number maximum is often referred to as the solar activity maximum. The solar activity changes with the solar cycle with a period of about 11 years. In the beginning of a solar cycle (solar activity minimum) sunspots appear at mid-latitudes on both hemispheres. With time the number of sunspots increases, and they move closer to the equator as the solar activity maximum approaches. After the maximum occurrence the sunspot number decreases until the solar activity minimum of nearly no sunspots is reached. Since the orientation of the dipolar part of the solar magnetic field reverses from one cycle to the next, the entire magnetic solar cycle is actually 22 years.

Table 1 shows the dates of minima and maxima of the solar activity cycle since 1960 as determined by David H. Hathaway (cycle number 20 - 23). The prediction of the cycle number 24 maximum was recently published by NOAA (National Oceanic Atmospheric Administration) [33].

1.1.2 The magnetic field of the Sun

If we assume a spherically symmetric, radially expanding solar wind and a conserved magnetic flux, the magnetic field of the Sun can be expressed as

$$B_r = B_0(\frac{R}{r})^2. \tag{1}$$

So it would fall of as r^{-2}. But an additional complication is the rotating solar atmosphere induced by the rotation of the Sun. This leads to a magnetic field that behaves far away from the Sun as

- B $\rightarrow r^{-1}$ in the equatorial plane (spiral more tightly wound)
- B $\rightarrow r^{-2}$ in the direction of the poles.

Due to the rotation of the Sun the magnetic field lines attain a spiral shape close to the Sun. The magnetic field is frozen into the plasma which is ejected from the base of the corona. The field lines carried through the interplanetary space become more tightly wound with increasing distance from the Sun. The calculated angle between the magnetic field direction and a line between the Sun and an observer at the orbit of the Earth is close to 45 degrees. If a strong dipole magnetic field is assumed for the Sun, all field lines are closed. Each line leaves the base of the corona, extends ($<$ 2 solar radii) into space and returns to the base of the corona on the other side of the solar equator.

For a weak magnetic field strength one would expect the corona to expand outward and to drag the frozen-in magnetic field with it. Since the solar magnetic field is not exactly a dipole field some field lines are open and are drawn outward by the expanding plasma. These field lines originating from high-latitudes of the Sun and the coronal plasma in that volume forms the solar wind. The two open field lines at a latitude of 45 degrees (calculated from isothermal magnetohydrodynamic models) on opposite sides of the dipole equator meet at low latitudes and extend outward nearly parallel to the equator. Since these two field lines come from opposite ends of the dipole, they have different polarities. So the polarity of the distant magnetic field must change sign at the equator. This fact implies a thin region of high current density

$$\vec{j} = \frac{1}{\mu_0}\vec{\nabla} \times \vec{B} \tag{2}$$

with $\vec{j}$ perpendicular to the field lines. It is the interplanetary current sheet that separates the fields and plasma flows from opposite polarities in the dipole field. The same feature can be found in the magnetotail of the Earth as explained in Section 1.4.2.

The left panel of photograph Fig. 2 is taken during solar eclipse. The white light does not come from coronal emissions, but is photospheric light scattered from the coronal gas. The bright structures at the right and lower left are closed magnetic field regions, often called coronal helmet streamers. They usually lie above the

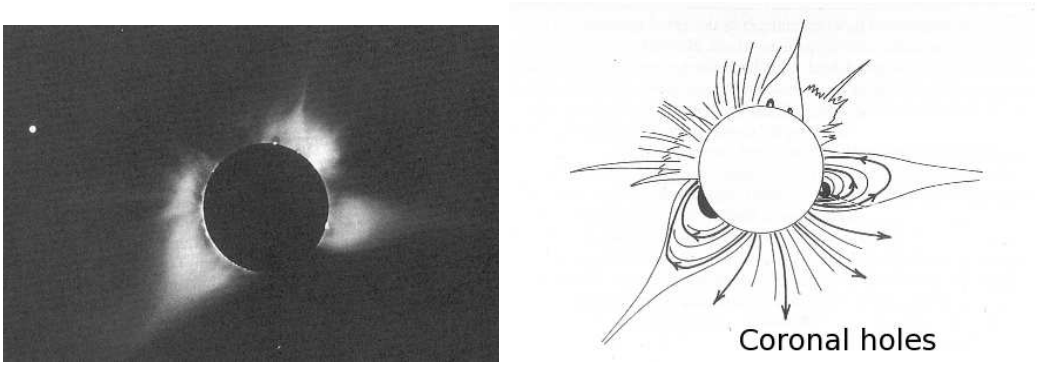

Fig. 2: The Sun and its different features [9]

neutral line, which is the region where the field polarity changes: On one side of the neutral line the magnetic field is directed away from the Sun, while on the other side of the neutral line the magnetic field is directed towards the Sun. The dark features in the bottom of the photograph are open magnetic structures known as coronal holes. The coronal holes are regions of low density, and so are the co-rotating high-speed streams which have their origin in the coronal holes. Coronal holes can remain stable for many months.

1.2 The interplanetary medium

The interplanetary medium is filled by the solar wind out to its boundary; the heliopause. Space between the planets is exceedingly tenuous. There are about five million electrons and five million protons per cubic meter in the solar wind near the Earth, while in our air at sea level there are $2.5{\cdot}10^{25}$ molecules in a cubic meter.

The magnetic field in the solar corona is approximately 10^5 nT, while the interstellar medium shows only 0.5 nT [6]. At the Earth orbit, the interplanetary magnetic field has an average strength of about 5 nT. By way of comparison, the magnetic field on the surface of the Earth is about 50'000 nT.

The characteristics of the interplanetary magnetic field, arising from the solar magnetic field carried by the solar wind, change depending on the 11-year cycle of the activity of the Sun. About 1 million tons of material is transported away from the Sun every second. Whenever the Sun is active, large bursts of plasma with intense field structures can be seen in the interplanetary space, which can be treated as a magnetohydrodynamic (MHD) plasma flow. A plasma is an ionized quasi-neutral gas, containing enough free charges to move (among others) under the influence of collective electromagnetic phenomena. Already if one percent of the gas is ionized, it behaves like a plasma [21]. The plasma itself is electrically neutral and its existence is only possible by balance of ionization and recombination. If a gaseous plasma cools, charged particles recombine and it ceases to be a plasma.

There are three distinct components of the solar wind in the interplanetary medium

- High-speed streams from coronal holes
- Slow, dense, cool flows near the heliospheric current sheet
- Transients associated with solar flares and coronal mass ejections.

HSSs have a higher kinetic temperature than the other structures, eventhough their ionization temperature is lower, because they originate in cool holes on the Sun. There is evidence that low solar wind speeds are measured near the solar equator while at higher heliographic latitudes higher values are observed. As the solar wind expands in all directions, the density varies as $N \propto R^{-2}$, where R is the radial distance from the Sun.

1.2.1 The solar wind properties and the Parker model

E. Parker showed in 1958 [17] that an equilibrium between the Sun and the interstellar medium is impossible for a static corona, which is why he proposed the existence of an outward expanding solar wind. Already in 1951, Biermann [4] proposed by looking at a comet tail that abrupt changes in the outflow of material could only be explained by the existence of a particle outflow from the Sun. The solar wind is a result of a vast difference in gas pressure between the solar corona and the interstellar space that is only restrained by the influence of the gravity of the Sun. Typical observed properties of the solar wind at 1 AU from the Sun are shown in Table 2.

Table 2: Slow and fast solar wind properties at 1 AU from the Sun

	Slow solar wind	Fast solar wind	
Proton density N:	$10.7\,\mathrm{cm}^{-3}$	$3\,\mathrm{cm}^{-3}$	[11], [22]
Flow Speed (nearly radial):	348 km/s	667 km/s	
Magnetic Field:	3 nT	6 nT	

The solar wind is fast and tenuous. It consists mainly of ionized hydrogen with a small amount of ionized helium and some heavier ions. The viscous force is negligible everywhere in the solar wind, except of some small regions like in shock waves [6]. Most of the momentum and kinetic energy of the solar wind is carried by protons due to their larger mass. The dynamic pressure for the slow and fast solar wind

$$p_{dynamic} = \frac{1}{2}\rho \cdot \vec{v}^2 \cong 2.2\,\mathrm{nPa}$$

arising from the radial momentum flux varies typically between 1 and 10 nPa, where ρ is the mass density. The plasma thermal pressure (gas pressure) is given by

$$p_{Gas} = nk(T_p + T_e) \tag{3}$$

where k is the Boltzmann constant and indices p and e indicate protons and electrons, whose temperatures at 1 AU are around the values shown in Table 3.

Table 3: Slow and fast solar wind temperatures at 1 AU from the Sun

	Slow solar wind	Fast solar wind
Proton temperature T_p:	$5.5 \cdot 10^4$ K	$2.8 \cdot 10^5$ K
Electron temperature T_e:	$1.9 \cdot 10^5$ K	$1.3 \cdot 10^5$ K

[22]

For the gas pressure can be calculated

$$p_{Gas} = nk(T_p + T_e) \cong \begin{cases} 36\,\text{pPa for the slow solar wind} \\ 17\,\text{pPa for the fast solar wind} \end{cases}$$

Together with the mass density $\rho = N(m_p + m_e)$, the speed of sound waves becomes

$$c_s = \sqrt{\frac{\gamma \cdot p}{\rho}} \cong \begin{cases} 58\,\text{km/s for the slow solar wind} \\ 75\,\text{km/s for the fast solar wind} \end{cases}$$

in case of ionized hydrogen, where the ratio of specific heats at constant pressure and constant volume is $\gamma = \frac{5}{3}$. These sound speeds are much smaller than the speed of the solar wind. Therefore the solar wind at 1 AU is highly supersonic. For the slow and fast solar wind values from Table 2, the magnetic field induces a magnetic pressure at 1 AU of

$$P_{mag} = \frac{B^2}{2\mu_0} \cong \begin{cases} 3.6\,\text{pPa for the slow solar wind} \\ 14\,\text{pPa for the fast solar wind} \end{cases}$$

where μ_0 is the permeability of the free space. The ratio of gas pressure (thermal pressure) and magnetic pressure P_{mag} indicates the equal importance of both pressure components in the solar wind. It is denoted as β and varies at 1 AU between 0.3 – 3. The corresponding waves of the magnetic field in a well-conducting plasma are small amplitude waves that are driven by magnetic fluctuations. They are known as Alfvén waves and propagate at about the same speed as the sound waves. The Alfvén speed is

$$V_A = \frac{B}{\sqrt{\mu_0 \rho}} \cong \begin{cases} 20\,\text{km/s for the slow solar wind} \\ 76\,\text{km/s for the fast solar wind} \end{cases}$$

where ρ is the particle mass density. The total solar wind speed is typically 400 – 700 km/s and thus nearly always super-Alfvénic.

Models that extend the magnitude of the magnetic field of the Sun observed at the visible surface into the corona predict an average field strength of a few tenths of a mT at the coronal base. This would result in a magnetic pressure of $p_{mag} \cong 10$ mPa, which is far greater than the gas pressure. The consequence of this are Alfvén waves that travel several times faster than ordinary sound waves in the corona.

1.2.2 The heliospheric current sheet

The heliospheric current sheet (HCS) is created where open field structures with opposite magnetic polarities approach closed magnetic regions. It thus has its footpoints at the neutral line of the Sun near the magnetic equator (see Fig. 3), which it maps to the heliosphere. The HCS co-rotates rigidly with the Sun. Its form is slightly asymmetric: It extends to higher latitudes in the south than in the north. Small-scale fluctuations arising from the turbulent medium surrounding the HCS and other perturbations cause a very highly complex shape of the HCS. Because the solar dipole axis is tilted, a stationary observer near the solar equator is alternately above and below the current sheet and thus alternately in two regions of opposite magnetic polarity. This is also what can be observed from Earth. Since the Sun has a more complicated magnetic field than that of a magnetic dipole, the current sheet crossings can be more frequent.

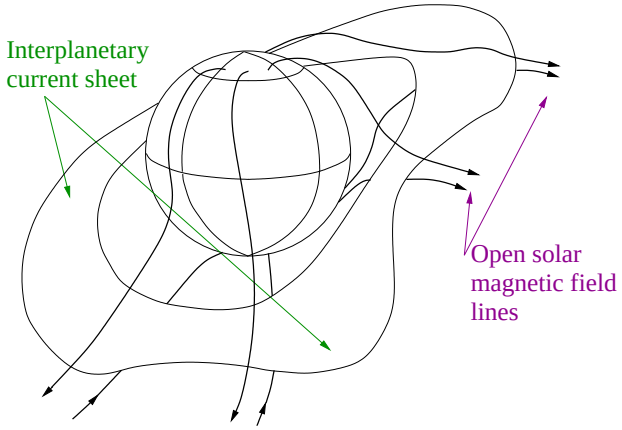

Fig. 3: The heliospheric current sheet called the ballerina skirt by Parker.

One consequence of the 11-year solar activity cycle is a clear change in the solar magnetic field. During the ascending solar activity phase the large scale dipole field is found to be in a disorganized state. There are up to four wraps in the current sheet. In times of a solar activity maximum the structure is much more complex and multiple current sheets appear. Coronal holes are observed at any solar latitude. The ejecta causes displacements of the HCS. After the activity maximum, a new dipole field with an opposite polarity develops. As the activity decreases, the dipole strength increases. Close to the solar activity minimum, a two-sector structure in the ecliptic plane of the HCS can be observed. Thus, the radial dependence of the HCS at any given time is caused by time variations of the neutral line, meaning the solar activity at the solar surface.

Near the HCS the solar wind density is generally high, the temperature low and the speed also low. In contrast at declining solar activity low densities and high temperatures in the solar wind are observed, which is associated with co-rotating streams embedded within the slow solar wind.

1.2.3 High-speed solar wind streams

The 27-day solar rotation period induces a large change in the solar wind speed as the heliospheric current sheet passes an observer in the ecliptic plane. The velocity increases from 300 – 400 km/s to about 700 km/s after the magnetic polarity has changed the sign at the sector boundary. The mean velocity increases toward the centre of the sector and then decreases toward the crossing of the next sector boundary. Each sector has a certain polarization [9].

These structures of increased velocity are called high-speed streams. High densities can be observed every time a sector boundary is crossed, and shortly after that, there is a sudden increase in the velocity (see plots in Section 3 and compare also with explanation in Section 5).

1.2.4 Co-rotating streams

Co-rotating streams are in close relation to high-speed streams. These streams tend to occur every 27 days with a relatively low density in the stream itself, but relatively high density and magnetic field strength ahead of the stream. Also the total pressure in co-rotating stream interaction regions consisting of P_{Gas} and P_{mag} reaches values of 2 to 10 times the value at 1 AU, which is on average (220 ± 30) nPa.

What are co-rotating streams?
Already in 1964 Billings and Roberts [5] introduced the idea that the sources of co-rotating streams are regions of open magnetic field lines which extend from the photosphere to the interplanetary medium. Krieger et al. stated in 1973 [10] that co-rotating streams are coronal holes in which the magnetic field lines are open (as already mentioned in Section 1.2.1). This explains the fact of a constant polarity in co-rotating interaction regions that are produced by co-rotating streams as we will see in a short while.

The shape of the Parker spiral arms depend on the solar wind speed. Solar wind streams emitted from different regions of the solar corona have different speeds: The edges of the polar coronal holes and coronal holes elsewhere than at the poles emit slow winds with velocities around 400 km/s, whereas the polar coronal holes emit faster winds with velocities of about 700 km/s (as measured by the Ulysses spacecraft during its two revolutions around the solar polar regions). For the fast solar wind flow the spirals are less wound than for slow solar wind flow. Because of the rotation of the Sun, the fast solar wind catches up with the slower solar wind ahead (Fig. 4). The interaction regions between co-rotating streams are called co-rotating interaction regions (CIRs) [21]. This feature can be seen in the profile of high-speed streams: A rapid rise in velocity and a slow decay due to the subsequent slower solar wind. The fast solar wind is what can be seen shortly after the interaction region. Ahead of it is the slow solar wind. Interaction regions are present at all times ahead of co-rotating streams at 1 AU. The leading edge of a CIR is a forward pressure wave that propagates into the slower plasma ahead, while the trailing edge is a reverse pressure wave that propagates back into the high-speed flow.

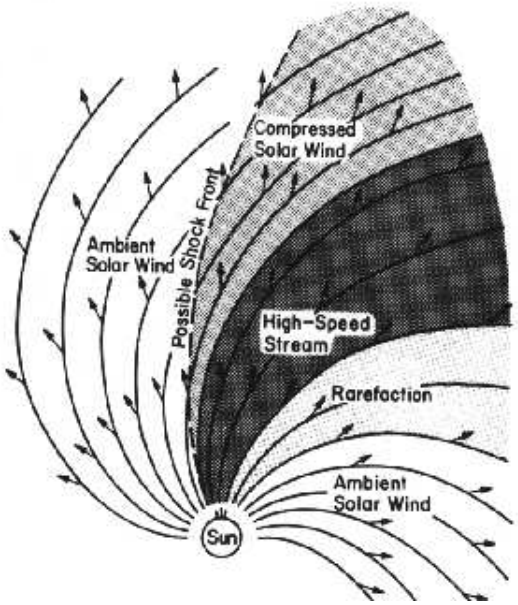

Fig. 4: Co-rotating interaction regions [8]

The process of fast plasma overtaking slow plasma ahead is mostly referred to as kinematic steepening [18]. A compression forms ahead of the HSS and a rarefaction on the trailing edge. It also leads to a compression of the magnetic field behind the slow stream. The compression is greatest near the solar equatorial plane, since the compression is caused by solar rotation, which is greatest near the equator. Hence there is no compression at the poles, where the effect of solar rotation is zero. The motion of the fast plasma behind the stream results in a rarefaction, because of a larger distribution of the volume in the back part of the radially moving stream (see Fig. 4). The interaction between the fast, but low density co-rotating stream and the slow, but high density stream ahead resembles a collision. A collision or a kinematic steepening causes an increase in the magnetic field strength, as the field is frozen into the plasma. Otherwise a kinematic rarefaction would cause a decrease in magnetic field strength.

Some models predict the existence of shocks at the compressed plasma front, where ions are locally accelerated to high speeds. But most CIRs do not have shocks at the Earth orbit but have steepened into shocks by 2 AU [24] and [1]. In this master thesis data are taken from the ACE satellite 1.5 million km away from the Earth or 0.99 AU from the Sun respectively and as a consequence nearly no CIRs with shock structures are observed. Near the solar minimum particles energized at CIRs are the dominant source of energetic particles with energies ranging from several keV to several MeV. These particles are a key factor in magnetic storms and substorms in the near-Earth space.

1.2.5 Magnetic clouds

Magnetic clouds are a subset of interplanetary ejecta of coronal mass ejections (CMEs) and thus they are not associated with high-speed streams. Their traveling time from the Sun to 1 AU is 3 – 4 days. They can be recognized as structures with

- enhanced magnetic field strength
- low temperature
- low density

But these conditions are only necessary, but not sufficient for the identification of a magnetic cloud. Magnetic clouds often move faster than the ambient medium

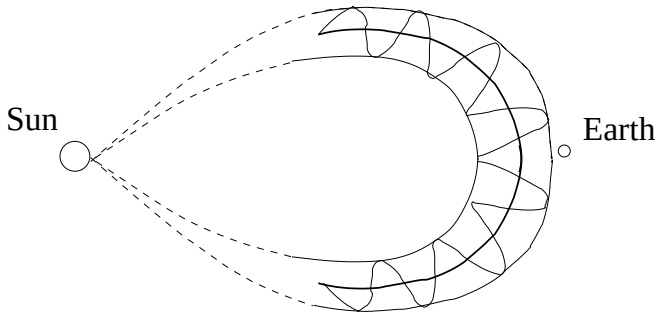

Fig. 5: The large-scale configuration of a magnetic cloud [6]. The dashed lines near the Sun are only to indicate that the magnetic cloud might be connected to the Sun at both ends of its tube-like form.

and therefore drive a shock ahead unlike HSS at 1 AU. Shock waves are transitions from super- to subsonic flow accompanied by compressions and dissipation [21]. A shock characteristic is a simultaneous increase in plasma speed, density, temperature and magnetic field strength [9]. Similar to high-speed streams the speed typically decreased across magnetic clouds. The radial extent of magnetic clouds is about 0.25 AU at the Earth.

1.3 The magnetic field of the Earth

1.3.1 The magnetic field of the Earth

The surface equatorial field strength of the Earth is 30'000 nT at the equator and 60'000 nT at the poles. It falls off in strength with increasing distance from the Earth. The magnetic field caused by the core of our planet is not the only one responsible for the irregularities of the field strength we measure on the ground.

There are four different sources that create the magnetic field of the Earth

- *The main field* is generated in the fluid core of the Earth by a geodynamo
- *The crustal field* comes from the magnetized rocks in the crust
- *The external field* is caused by electric currents in the ionosphere and in the magnetosphere. These currents are produced by the solar electromagnetic radiation and the solar wind interaction with the magnetic field of the Earth.
- *The inductive field* is generated by an electromagnetic induction process that is caused by electric currents induced in the crust and the upper mantle by the external magnetic field time variations. This happens because the Earth is an electric conductor, allowing electric current to flow [12].

The magnetic field of the Earth varies continuously with time. It is approximately a dipole field. The dipole is located at the centre of the Earth and has its axis almost parallel to rotation axis (11.5° difference). At present, magnetic north points towards geographic south and vise versa. In polar coordinates the dipole magnetic field is

$$\vec{B} = \frac{\mu_0}{4\pi}\frac{\vec{M}_E}{r^3}\sqrt{3\cos^2\theta + 1}. \tag{4}$$

where $\vec{M}_E$ is the magnetic dipole moment of the Earth, located in the origin.

1.3.2 The Geocentric Solar Magnetospheric coordinate system

The dayside of the Earth is defined as the Sun-facing side. The coordinate system that will be used throughout this thesis is the Geocentric Solar Magnetospheric System (GSM), where

- X-axis: Points from the Earth to the Sun
- Z-axis: Perpendicular to the x and in a plane that contains x and the dipole axis, positive pointing northward
- Y-axis: Completes the right-handed triad.

The point of origin is in the centre of the Earth.

1.4 Magnetohydrodynamics (MHD) in space plasmas

1.4.1 MHD equations and plasma description

The fundamental assumption is that the plasma coming from the Sun transported by the solar wind can be assumed to behave like a fluid described by hydrodynamics. In the presence of a magnetic field the behaviour of such a fluid changes and the applied theory is magnetohydrodynamics. Many of the models describing basic processes in the solar system are based on MHD: The outflow from the coronal holes, the behaviour of the heliospheric current sheet and the solar wind flow between the Sun and the Earth.

The MHD equations are a combination of fluid motion equations and the Maxwell's equations. On these equations bases the knowledge of processes in the interplanetary medium and on the Sun. Assuming that the plasma speed is much smaller than the speed of light one can neglect the displacement current. The ideal MHD equations describe a plasma in which the diffusivity of the plasma flow is omitted. It is a reasonable assumption in the case of the solar wind and in many regions of the magnetosphere. However, in the case of magnetic reconnection or the solar atmosphere, the diffusion plays an important role and ideal MHD is not applicable (see Section 1.4.2).

$$\frac{\partial \rho}{\partial t} + \nabla \cdot (\vec{u}\rho) = 0 \tag{5}$$

$$\rho \left(\frac{\partial \vec{u}}{\partial t} + \vec{u} \cdot \nabla \vec{u} \right) = -\nabla P + (\nabla \times \vec{B}) \times \vec{B}/\mu_0 + \vec{f}_{ext} \tag{6}$$

$$\frac{\partial \vec{B}}{\partial t} = \nabla \times (\vec{u} \times \vec{B}) \tag{7}$$

$$\frac{d}{dt} \left(\frac{P}{\rho^\gamma} \right) = 0 \tag{8}$$

Equation (5) is the continuity equation for the mass density, and $\vec{u}$ is the flow velocity. Equation (6) is the momentum equation. It follows from the Lorentz force acting on a quasi-neutral ($\rho_q = 0$) plasma element that carries a current. $\vec{f}_{ext}$ are the external forces that act on each particle (e.g. gravity). The induction Equation (7) is derived from Ampère's, Ohm's and Faraday's law and tells us how the vectors $\vec{B}$ and $\vec{J}$ evolve. To close the four equations, Equation (8), known as the energy equation, relates plasma pressure to mass density.

In this set of equations the induction equation (7) is especially important for the origin of interplanetary magnetic field lines, which is the solar dynamo. But since the magnetic diffusivity in the solar chromosphere is about 1000 and about 0.5 in the corona one cannot use ideal MHD to describe the processes. Thus the MHD induction equation becomes

$$\frac{\partial B}{\partial t} = \nabla \times (\vec{v} \times \vec{B}) + \eta \nabla^2 B \tag{9}$$

where $\eta = 1/\mu_0\sigma$ is the magnetic diffusivity, where μ_0 is the permeability of vacuum and σ is the electrical conductivity. The plasma velocity $\vec{v}$ includes differential rotation and convection in the Sun. If $\eta\nabla^2 B$, describing the diffusion of the field, is zero, the field is frozen-in to the plasma and moves with it. This term expresses that the magnetic flux through a closed circuit in the plasma frame of reference is constant. $\nabla \times (\vec{v} \times \vec{B})$ describes the plasma convection. Both terms on the right are needed to describe a plasma dynamo. Without diffusivity we would have no new flux creation. It is difficult to find solutions for both parts of the equation together, therefore, extensive computer simulations have been developed to address the issue.

Why can MHD be applied for the solar wind? What does justify this?
Because there are differences between the plasma components, it is required that the time-scale of the variations of the fluid and fields must be longer than the time-scale of the heaviest particle component. This implies that *the characteristic frequency ω of any change in the plasma must be smaller than the helium ion cyclotron frequency ω_{c_i} in the solar wind.* The cyclotron frequency or gyrofrequency is defined as

$$\omega_c = \frac{qB}{m} \tag{10}$$

and has opposite signs for positive and negative charges. For ionized helium ions (He^{2+}) $\omega_{c_i} \cong 0.14\,\mathrm{s}^{-1}$ if a magnetic field of 3 nT is assumed. The characteristic frequency can be determined from the velocity variation timescales. The condition $\omega < \omega_{c_i}$ is fulfilled under most circumstances in the solar wind.

A second condition is that *the characteristic length scale L must be longer than the ion gyroradius.* The gyroradius of a particle is defined as

$$r_c = \frac{mv_\perp}{|q|B} \tag{11}$$

which includes the gyrofrequency. Assuming an ideal gas one gets a thermal velocity of

$$v = \sqrt{\frac{3k_B T}{2m}} \cong 30\,\mathrm{km/s} \tag{12}$$

if the fast solar wind temperature for protons is taken to be about $2.8 \cdot 10^5\,\mathrm{K}$ (by using the values of Table 2) and the mass of a helium ion He^{2+}. This then results in

$$r_c = 205\,\mathrm{km}. \tag{13}$$

The characteristic length scale L is the considered scale for the research of high-speed streams. A reasonable value is the size of the magnetosphere which is approximately 70'000 km on the dayside of the Earth. This is the distance that particles at least have to cover in order to reach the Earth after arriving at the magnetopause. As clearly can be seen, L is much longer than the gyroradius and thus MHD is applicable.

To make use of MHD, the solar wind can, in a very good approximation, be described as a fully ionized plasma that moves radially away from the Sun. The solar wind is a highly conductive plasma. It transports away the solar magnetic field as a frozen-in field. This concept results from Ohm's law

$$\vec{j} = \sigma(\vec{E} + \vec{v} \times \vec{B}) \tag{14}$$

where the $\vec{v}$ is the flow velocity, σ is the conductivity, $\vec{E}$ is the electric field and $\vec{B}$ is the magnetic field. If the plasma is collisionless, σ is infinite. The only equation that in this case fulfills this condition is

$$\vec{E} + \vec{v} \times \vec{B} = 0 \tag{15}$$

or

$$\vec{E} = -\vec{v} \times \vec{B}. \tag{16}$$

This is the frozen-in-flux condition, meaning that the magnetic flux is frozen into the fluid flow. The upper equation also states that since the cross-product between the velocity component parallel to the magnetic field is zero, the electric field parallel to the magnetic field must vanish in such a plasma.

1.4.2 Magnetic reconnection

Magnetic reconnection is a phenomenon where the diffusivity of the plasma flow cannot be neglected, thus ideal MHD is not a valid description of the reconnection process. At the dayside magnetopause magnetic reconnection occurs when the in-

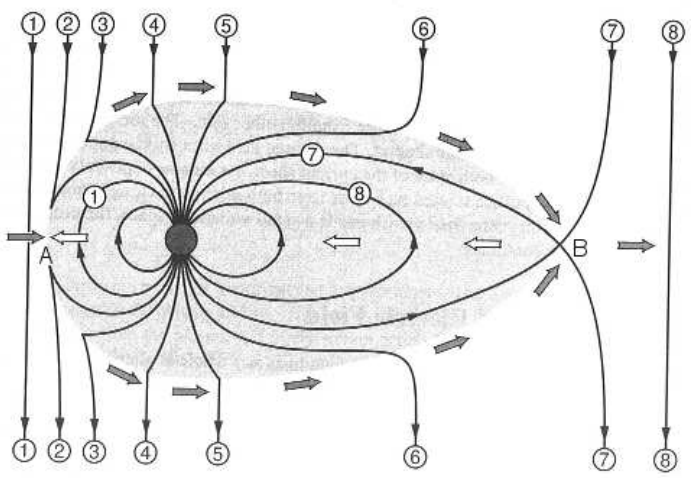

Fig. 6: Reconnection with an interplanetary field northward component [2]

terplanetary magnetic field has a southward component. As the terrestrial magnetic field is northward there, the two magnetic fields point in opposite directions (see line

1 in Fig. 6). Two oppositely directed magnetic fields form a current sheet between them. Plasma flows toward the sheet from the right and left. At the magnetopause the plasma inflow coming from the lefthandside (denoted by a shaded arrow on the left in Fig. 6) comes from the solar wind, transporting for instance CIRs or other intense magnetic structures to the magnetopause. The plasma inflow on the right is a consequence of another reconnection process in the magnetotail that creates the magnetospheric convection pattern as described in Section 1.4.4.

At the magnetic X-point of the reconnection region (as can be seen in Fig. 7 in the middle panel) the two fields annihilate and the topology of the magnetic field changes. The arrows denote the plasma flow. In the real magnetosphere the magnetic field normal component does not vanish and thus the flux normal to the surface is not zero. That means that matter from the magnetosheath - surrounding the magnetosphere - can penetrate into the magnetosphere along the magnetic field lines. The two oppositely directed field lines that first become connected are now convectively transported tailward after splitting into two open field lines, marked in Fig. 6 with (2). One end is still connected to the Earth, the other stretching out into the solar wind. The field lines move across the polar cap (3 – 6) into the tail (shaded region in Fig. 6). In the nightside reconnection takes place when the two open field lines meet (7 and 8). This occurs about $100-200\,R_{\oplus}$ away from the Earth. The particle flow is thus from north and south towards the tail current sheet, and after the magnetic reconnection has taken place a flow towards and away from the Earth emerges. Plasma is thereby transported Earthward and arrives after flowing past the terminator at the dawn and dusk to the dayside, where it finally participates in another reconnection process at the dayside. In three dimensions, the tail magnetic reconnection does not occur at a singular point, but rather at a line, which is then instead of X-point called X-line.

It is crucial to mention that magnetic reconnection can also take place if the interplanetary magnetic field has a northward component. The fundamental requirement for magnetic reconnection to occur is an interplanetary magnetic field component that points in the opposite direction of the terrestrial field. So reconnection may happen at many different places of the magnetopause simultaneously, but the plasma input efficiency is highest on the dayside magnetosphere.

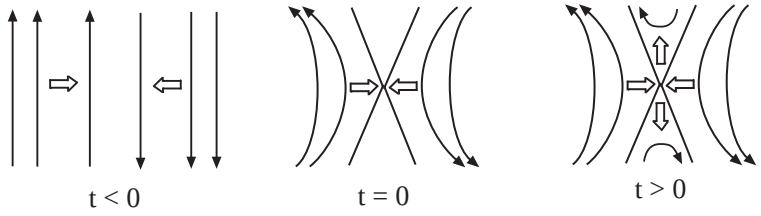

Fig. 7: Schematic model of the magnetic reconnection process. Such a topology exists for instance at the magnetopause (denoted by A in Fig. 6) or in the magnetotail sheet (B in Fig. 6. Picture by Eija Tanskanen)

Magnetic reconnection itself violates the frozen-flux theorem which claims that the fluid flow through a surface remains constant, even if the surface changes its shape or location. Since the plasma and the field lines are on both sides flowing toward the current sheet, the reconnection configuration is not stable due to collisions or other diffusive processes the magnetic field can disappear in a particular point because of diffusion. This leads to an X-point as can be seen in Fig. 7 in the middle panel. In the X-point the magnetic field is zero. After this crossing the antiparallel field lines are cut and reconnected with the part from the other side as illustrated in the last panel of Fig. 7. The emerged field lines are now populated with plasma from both sides of the current sheet and the merged field line are pushed away from the X-point in the direction of the resulting magnetic field (black thin arrows in the picture). There are different models for the process of magnetic reconnection, like the Sweet-Parker model or the Petschek model. For further details I refer to a book written by M. G. Kivelson and C. T. Russell [9].

1.4.3 The Solar wind - magnetosphere interaction

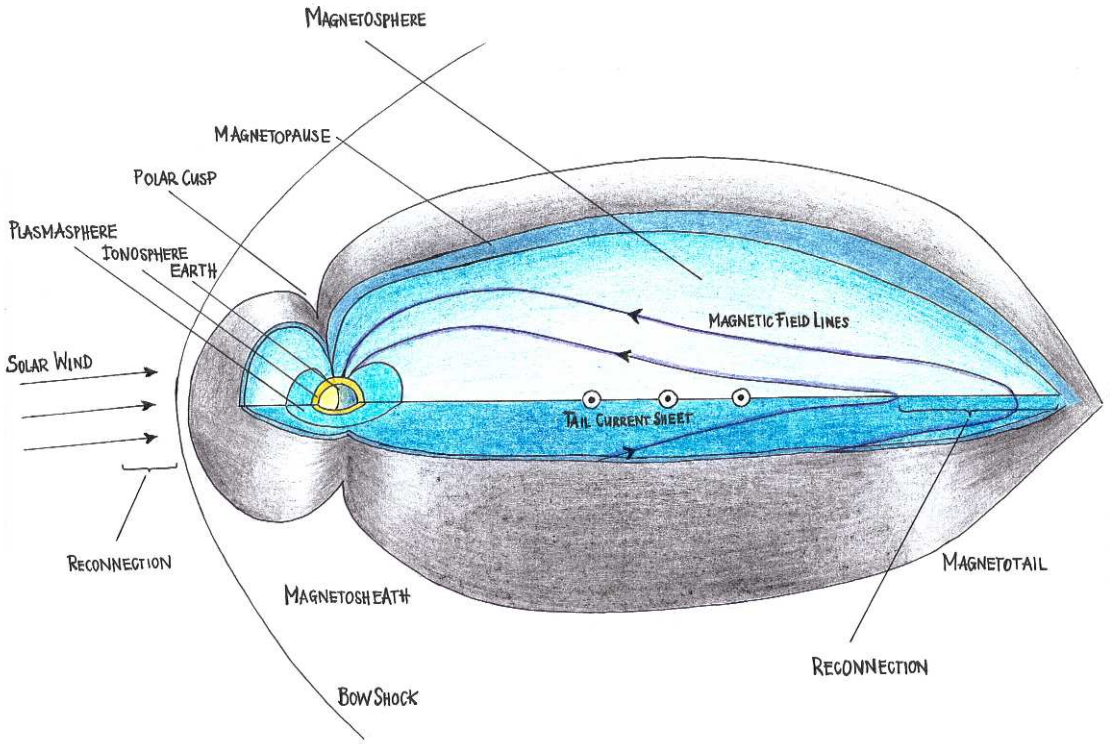

Fig. 8: Three dimensional view of the magnetosphere

The solar wind with the embedded interplanetary magnetic field comes supersonically from the Sun through the interplanetary medium to the Earth in about

3.5 days. Upstream of the Earth, it collides with the magnetosphere, forms a bow shock, compresses the magnetic field on the dayside and stretches it to a very long magnetotail on the nightside (Fig. 8). The magnetosphere is simply defined as the area around a body that is controlled by its magnetic field. This magnetosphere protects us from energetic solar particles. But some of the energetic particles manage to penetrate the magnetopause. There are a few millions of protons and electrons in every cubic meter of the magnetosphere and the magnetic field strength ranges from 1 to several times ten nanotesla.

The fully ionized and magnetized solar wind plasma cannot mix with the terrestrial magnetic field. This follows from the frozen-in concept, which assumes that the magnetic diffusion is negligible, and thus no electrical resistance is present. Instead of mixing, the magnetosphere will be compressed toward the Earth by the dynamic pressure of the solar wind. The magnetopause forms at the location where the solar wind and magnetosphere plasmas are in pressure balance. One can calculate the distance of the magnetopause from the Earth to be about 10 Earth radii ($1\,\mathrm{R}_\oplus \cong 6370\,\mathrm{km}$) under normal conditions.

At high latitudes the magnetopause is discontinuous at one location. This is identified as the polar cusp (see Fig. 8) that arises from the geometry of the dipole field. The polar cusp is magnetically connected to the boundary of the polar cap. At lower latitudes is the auroral oval, an approximately circular band around the two geomagnetic poles within which most of the auroral activity occurs. The ionosphere, a part of the upper atmosphere below the magnetosphere, is created by solar ultraviolet and X-ray radiation and varies dramatically with the solar activity. It is the transition region from the fully-ionized magnetospheric plasma to the neutral atmosphere. It is a mixture of plasma and neutral particles. Eventhough most of the ionosphere is gravitationally bound to the Earth, some particles have enough energy to escape to the magnetosphere. Oxygen ions, protons and electrons from the ionosphere are trapped by the magnetic field of the Earth and form the plasmasphere extending outward to between $4-6\,R_\oplus$ depending on magnetic activity conditions.

1.4.4 Convection

The reconnection efficiency at the dayside magnetosphere depends on the orientation of the interplanetary field that interacts with the dayside magnetopause. When reconnection occurs on the dayside magnetopause, the opened magnetic field lines are swept tailward by the solar wind. The solar wind generates an electric field inside the magnetosphere, which is directed from dawn to dusk in the equatorial plane. The current in the magnetotail current sheet, separating two opposite directed magnetic field lines in the tail (see Fig. 8), is also directed from dawn to dusk (see Fig. 9).

The magnetic field of the Earth points northward, the global electric field from dawn to dusk, thus the plasma convection in the magnetotail points Earthward

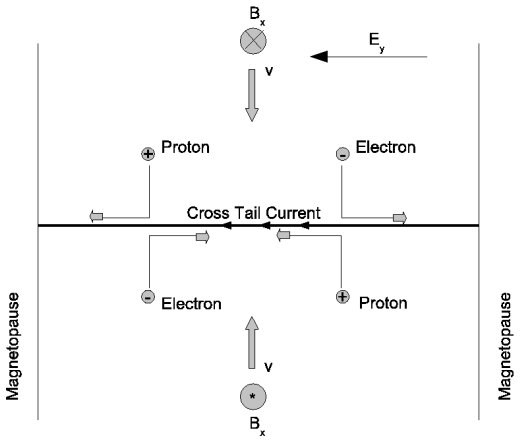

Fig. 9: The tail current seen from the nightside toward the Earth

because of the $\vec{E} \times \vec{B}$ drift

$$\vec{v}_E = \frac{\vec{E} \times \vec{B}}{B^2}. \tag{17}$$

The plasma flows past the Earth back to the dayside. With the plasma also the magnetic field lines move this way. This flow process is mapped from the magnetosphere down to the ionosphere at about hundred km altitude above the surface of the Earth. The ionospheric convection pattern is shown in Fig. 10.

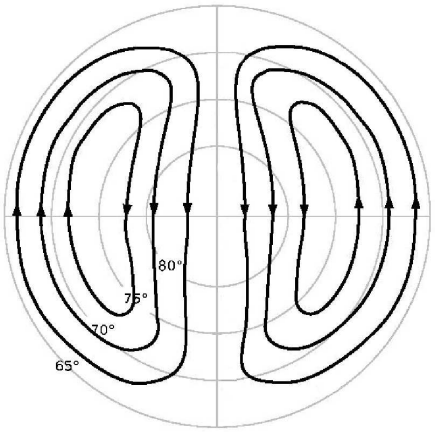

Fig. 10: The plasma motion within the high-latitude ionosphere generates a two-cell convection pattern. The dayside is orientated toward the top of the page. Picture adapted from [30]

Currents flow in to the weakly collisional ionospheric plasma. Because the magnetic field lines are equipotentials, the electric field in the magnetotail is mapped along the field lines to the auroral ionosphere. Electrons and protons both move under the $\vec{E} \times \vec{B}$ drift, but ions collide more frequently than electrons with atmospheric neutrals. This leads to a current flowing in the $\vec{E} \times \vec{B}$ drift direction.

These currents flow down from the magneto- to the ionosphere, along the auroral oval and up on the other side of the oval. They are concentrated in the auroral oval due to the much higher conductivity induced by the higher plasma densities. The current pattern forms two electrojets (flowing eastward and westward) called convection or auroral electrojets. The diameter of the auroral ovals depends on the amount of the open flux in the polar cap: during high geomagnetic activity the auroral oval expands to lower latitudes (see Fig. 11).

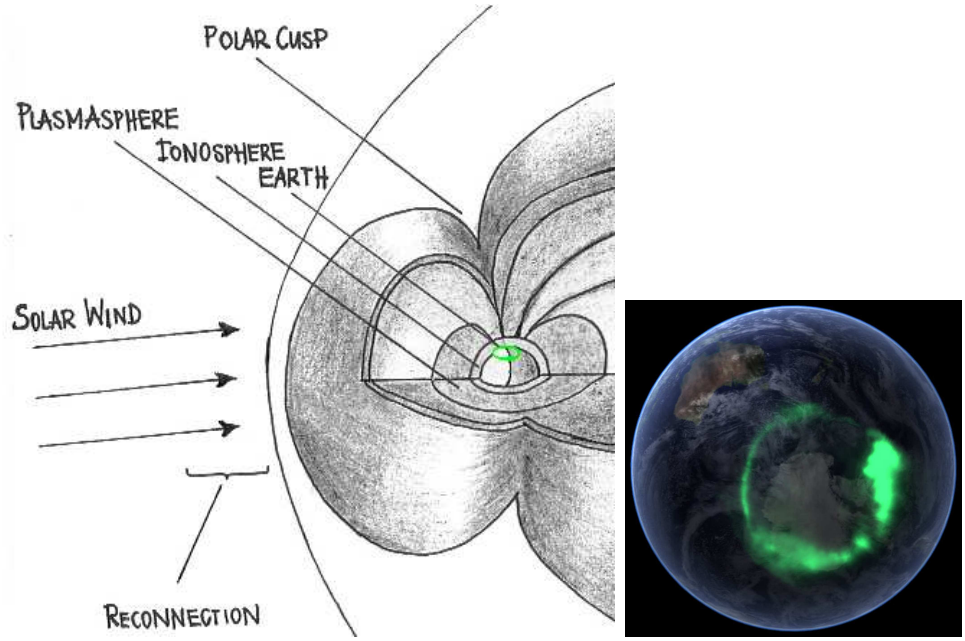

Fig. 11: Aurora in [26]

1.4.5 Magnetospheric substorms and Aurora Borealis

Changes in the previously mentioned currents are reflected as changes in the magnetic field on the surface of the Earth, called geomagnetic activity. To describe changes in the magnetic field of the Earth, magnetic-activity indices like the AE index (see section 1.4.6) are used. Substorms are the most frequent type of geomagnetic activity and produce magnetic field variations on Earth of typically a few hundred nanoteslas. They cause magnetic and auroral activations at high latitudes (auroral zone) where the currents intensify.

In the research of substorms high-speed streams are of high importance, since HSSs can transport magnetic structures to the magnetopause that enhance the reconnection rate in the dayside. Due to the 27-day periodicy of high-speed streams there is also a 27-day periodicity of substorms noticeable when the high-speed streams are prevalent.

The substorms are initiated when the dayside magnetic reconnection is enhanced. Reconnected magnetic flux is transported to the tail, and another reconnection region is formed in the magnetotail. This forces the flux to convect back to the dayside. However there is no need for identical or instantaneous dayside and nightside reconnection: An instantaneously higher reconnection rate in the dayside as compared to the nightside causes energy storage in the magnetotail. This is the beginning of

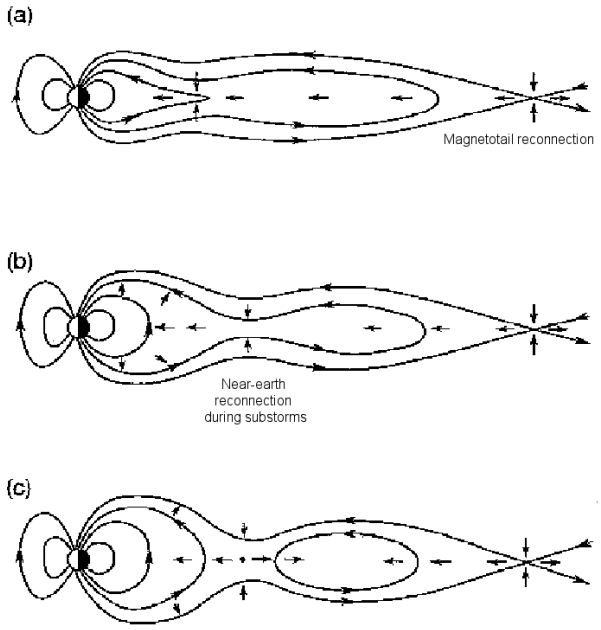

Fig. 12: The phases of a substorm

a substorm. The strength of the magnetic field and the magnetic flux density in the magnetotail are enhanced and the energy from the solar wind is added to the tail. During that time auroras appear in the form of auroral arcs. The magnetotail stretches and the dayside magnetopause moves closer to the Earth (see Fig. 12 panel (a)). The tail suddenly becomes unstable and tries to get rid of the stored energy. On a timescale of minutes, the stretched field lines collapse causing plasma jets toward the Earth and outward (see Fig. 12 panel (b)). This disruption of the near-Earth magnetotail field lines at $6-10\,R_\oplus$ causes a strong compression and heating in the enclosed plasma. The blocked part of dawn-to-dusk tail current must find a new circuit and is connected to the ionosphere circuit (Fig. 13). The electrons flowing into the auroral region along the field lines cause a sudden brightening of the auroral arcs; first in the midnight sector, but then in particular westward. The large region

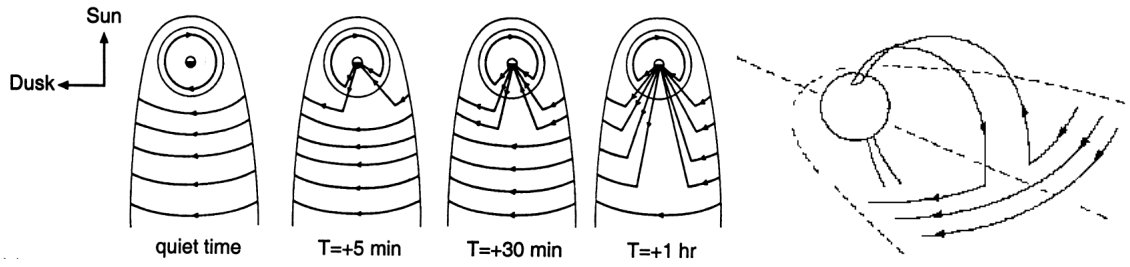

Fig. 13: On the left: Disruption of the tail current and evolution in the current systems. On the right: Field aligned currents connecting the magnetosphere with the ionosphere during substorms

between the near-Earth reconnection neutral point and the distant tail reconnection region in the magnetotail forms a plasmoid that is ejected anti-sunwards (see Fig. 12 panel (c)).

Atoms in the upper atmosphere are excited by collisions with the electrons coming from the tail current at altitudes above 100 km. The excitation later relaxes by ejecting photons which produce substorm auroras in altitudes between 95 and 150 km and lead to the formation of a substorm electrojet with strongly enhanced westward current flow in the midnight sector. The electrojet direction is determined by the current flow direction in the magnetotail (see Fig. 13 right hand panel). The current in the electrojets during substorms is generally much larger and more concentrated near midnight than during quiet times, during which only the convection electrojets are present (Fig. 14). The maximum current in the westward electro-

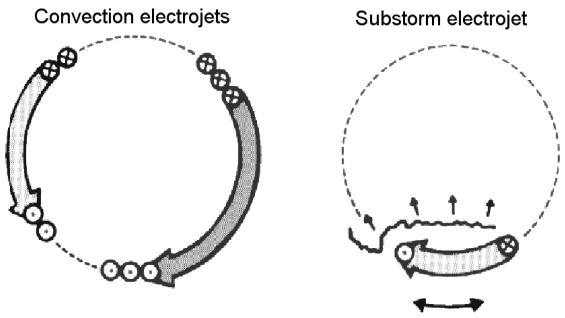

Fig. 14: The plasma and current flow in the auroral electrojets during quiet times and substorm times.

jet and thus the features of the substorm can be best determined by measuring the north-south horizontal disturbance in the magnetic field of the Earth. While the westward current creates a decrease in the horizontal component, an eastward current creates a corresponding increase.

Auroras are much stronger during a high solar activity. Their frequency of occurrence and intensity is closely correlated with the 27-day rotational period of the Sun and the 11-year sunspot cycle.

In summary, substorms and auroras depend on the plasma coming from the Sun (its magnetic field orientation), the magnetic field of the Earth, and the composition of the atmosphere. Additionally, the distribution of auroras depends on the different phases of the auroral substorm. Such substorm events usually occur several times in one day and last for about $1-2$ hours each.

1.4.6 The Auroral Electrojet (AE) index - consisting of AL and AU index

The AE index was introduced in 1966 as a measure of global electrojet activity in the auroral zone. The AE index is derived from the geomagnetic variations in the horizontal magnetic component (see Fig. 15) at 12 ground based observatories along the auroral zone in the northern hemisphere (Fig. 16).

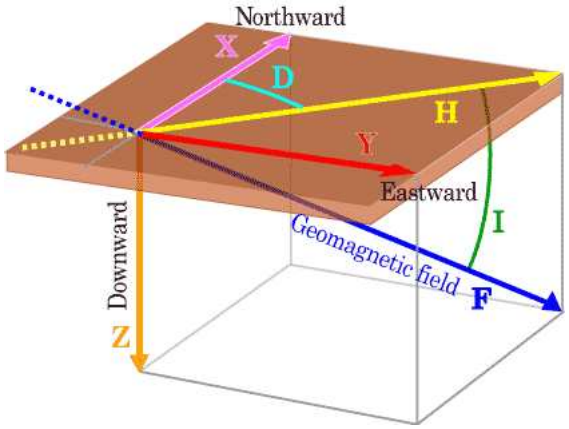

Fig. 15: The components of the geomagnetic field are: The declination (D), which is the angle between magnetic north and true north, and the inclination (I) which is the angle between the horizontal plane and the total field vector. The field intensity is generally expressed in units of nanotesla and described by the total intensity (F), horizontal component (H), vertical component (Z), the north (X) and east (Y) components of the horizontal intensity. Note: Downward means towards the centre of the Earth [28]

.

The data of the five international quietest days of every month are averaged and subtracted from each value of the one-minute data in this particular month. Then the largest and smallest values among the data from all observatories in each minute are taken as AU (A_{upper}) and AL (A_{lower}) indices, respectively. The difference, AU - AL, is defined as the AE index. AU and AL indices express the strongest current intensity of the eastward and westward auroral electrojets (currents), respectively. AE characterizes the global activity within the electrojets [28]. In the beginning of a substorm convection is enhanced. This causes an increasing current flow in the auroral electrojets, which is associated with a growing AE index and a decrease in the AL index due to the westward substorm electrojet. The AL index is of a higher importance for this study, because the main interests are in the currents that originate from the nightside of the Earth, from the magnetotail through processes driven by the southward interplanetary magnetic field.

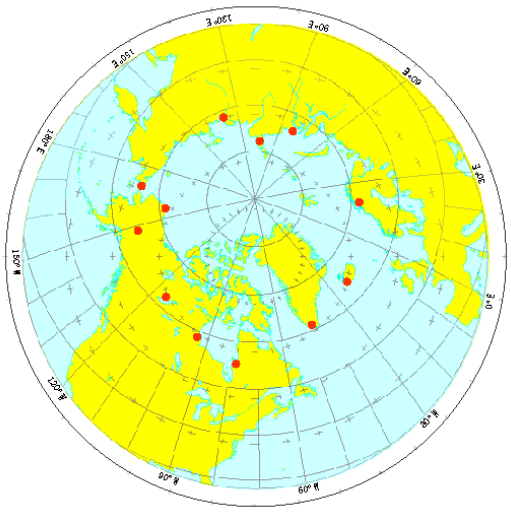

Fig. 16: Distribution of AE index observatories [28]

1.4.7 Solar cycle variations

In order to explain the periodicity for high-speed streams it is necessary to think about their origin. The source these streams lies in the regions of strong magnetic field in the chromosphere of the Sun. The high-speed solar wind streams do not show quite as clear period of 11 years as the sunspots, but already the first solar wind speed measurements during the declining phase of the solar cycle in 1962 (average speed 490 km/s) and in the next solar cycle in the years 1973 and 1974 (average speed > 500 km/s), higher speeds were measured than during other phases of the solar cycle. The same result was noted once again in the next solar cycle, in 1985. For three successive solar cycles the highest speeds occurred during the

declining phase of the solar activity. On the other hand, there is no evidence that the minimum speed would occur at a particular phase in the solar cycle.

1.5 Statistics

The Pearsons correlation coefficient q is a statistical measure for the correlation between two parameters. There is a positive correlation ($0<q<1$) if one parameter increases together with the other one. For negative correlations ($-1<q<0$) one parameter grows, while the other one decreases. In case that $q = 0$ there is no correlation and thus the two parameters are statistically independent of each other.

2 Data source - ACE spacecraft

The Advanced Composition Explorer (ACE) is a NASA mission mainly for sampling low-energy particles of solar origin and high-energy galactic particles. ACE makes measurements from an orbit around the L1 Lagrangian point, which is located between the Sun and the Earth about 1.5 million km from the Earth and 148.5 million km from the Sun. In this particular point the gravitational pull of the Sun and the Earth provide exactly the centripetal force such that the satellite has an angular velocity around the Sun equal to that of the Earth. Thus, the spacecraft remains between the Sun and the Earth at all times.

To give an idea where in the solar cycle ACE has taken measurements Fig. 17 illustrates the sunspot number based on data from the OMNI 2 database.

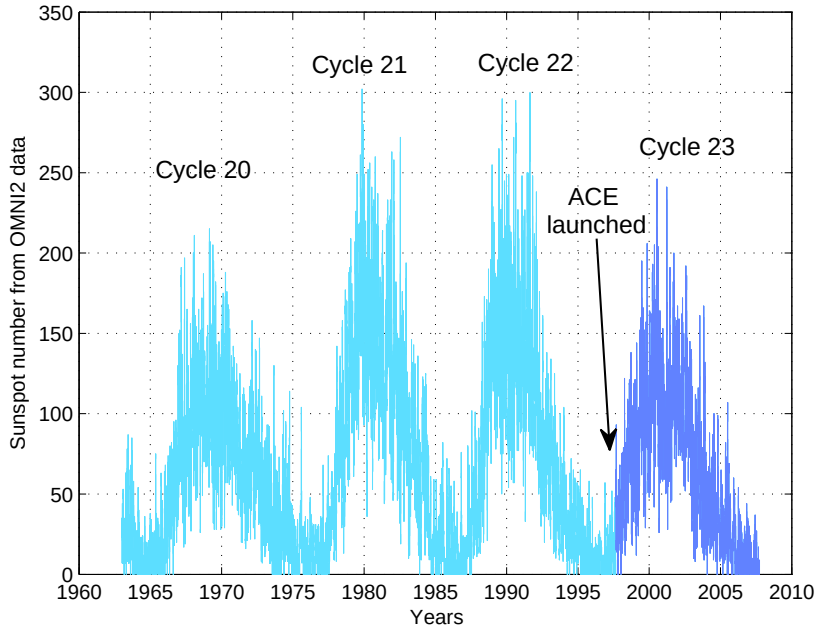

Fig. 17: The solar cycle and the time since ACE takes measurements

2.1 Technical specifications and instruments

The launch of the ACE spacecraft was on McDonnell-Douglas Delta II on August 25, 1997 from the Kennedy Space Center in Florida. This was during a solar cycle minimum. The planed mission lifetime was two years, but the propellant onboard

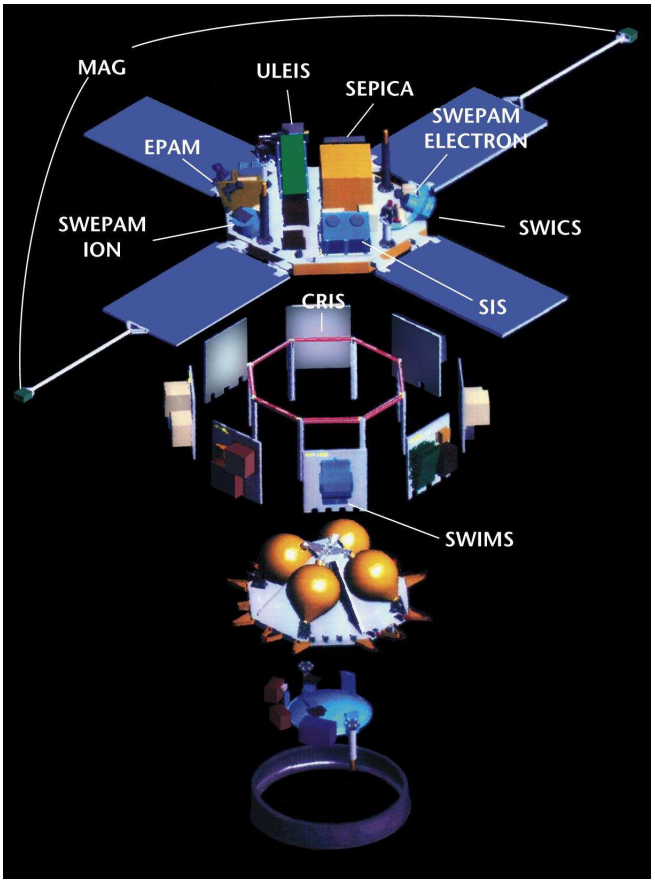

Fig. 18: Instruments on ACE [25]

can maintain the orbit around L1 until 2019. Since the L1 point is inherently unstable there have to be four to six maneuvers a year to keep the spacecraft in orbit around L1.

The ACE spacecraft is 1.6 m across and 1 m high and weighs 785 kg - including 189 kg fuel. The solar arrays generate approximately 500 Watts of power. ACE spins 5 times per minute with the spin axis pointed along the Earth-Sun line. The rotation of the spacecraft allows it to make measurements in all directions in the spin plane. The total aboard data storage is provided by two solid state recorders (2 Gigabits).

2.1.1 The magnetometer instrument - MAG [27]

This instrument measures the local interplanetary magnetic field direction and magnitude and its fluctuations as a function of time. It provides data down to 1 second averages. For high-speed stream analysis 16-seconds data are used, which is more manageable when treating larger scale structures.

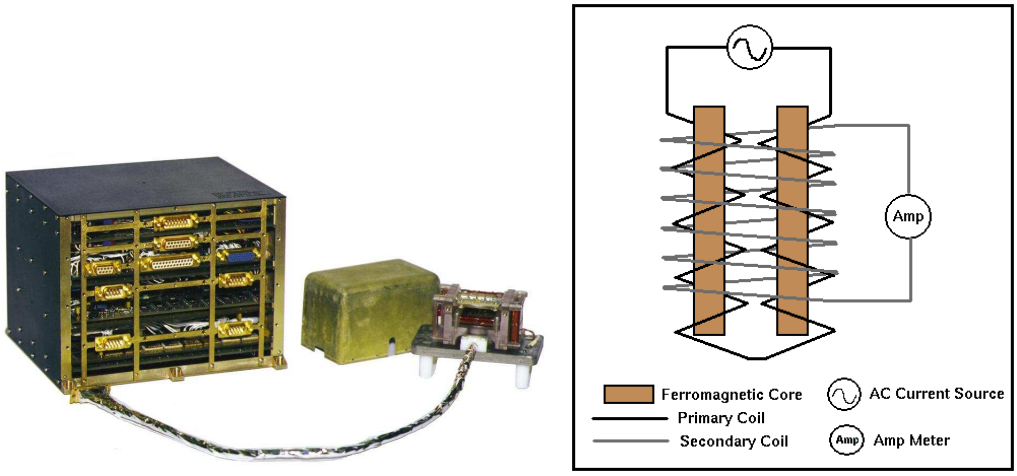

Fig. 19: MAG instrument [27] and the working principle of a fluxgate magnetometer [32].

The instrument is a fluxgate magnetometer (shown in a diagram in Fig. 19). Two sensors are mounted on a boom that is fixed at the opposite ends of the solar panels. A fluxgate magnetometer basically consists of two parallel ferromagnetic bars wound with a primary coil. An AC current through the primary coils causes magnetic fields in each coil, which are of the same strength but have opposite orientations. A secondary coil surrounds the two ferromagnetic cores and the primary coil. An external (for instance parallel) magnetic field reinforces the magnetic field of one core and reduces the other. This causes a voltage potential in the secondary coil that is measured. The measurement range of MAG is from $\pm 4\,\mathrm{nT}$ up to $\pm 65.536\,\mathrm{nT}$ per axis in eight discrete ranges.

2.1.2 The Solar Wind Electron, Proton, Alpha Monitor - SWEPAM

Fig. 20: SWEPAM instrument [34]

The SWEPAM instrument [34] measures the electron and ion fluxes of the solar wind plasma as a function of direction and energy. It gives the solar wind conditions every 64 seconds. The two sensors for the particle measurements are

1. Electron sensor that has a range of 1 to 1350 eV and uses an electrostatic analyzer, which measures $\frac{E_{kin}}{q}$ of each particle by bending their flight paths through the system.

2. Ion sensor measures particles with energies between 0.26 and 36 KeV and also computes the same energy to charge fraction with an electrostatic analyzer.

In an electrostatic analyzer an electric field is applied in a cylindrical condenser. The electric field exerts a force $\vec{F} = q \cdot \vec{E}$ on a particle with charge q. Using a magnetic field as a deflector, particles with specific values of $\frac{E_{kin}}{q}$ can be filtered.

3 The physics and properties of high-speed streams (HSS)

From this section onward the results of the own research on high-speed streams are presented. The data are either from the ACE spacecraft (all solar wind parameters) or from stations on Earth (AL index). The resolutions are for the ACE data 64 seconds (velocity, density) or 16 seconds (magnetic field). From the groundbased magnetometers one minute data are used.

3.1 The velocity distribution of HSS

Fig. 21 shows the velocity distribution in the Earthward x-direction for the years 1998 and 2003 together with a Gaussian fit. The velocity distribution of the slow solar wind follows the Gaussian distribution. The deviation from a Gaussian fit starts at around 500 km/s for both shown examples. A second non-Gaussian distribution overlaps and arises from there. This is the fast solar wind velocity distribution that includes the HSSs. Considering the years 1998 – 2006, the deviation from the main Gaussian fit starts between 490 km/s (in 2002) and 552 km/s (in 2004). The year 2003 (Fig. 21 lower panel) shows clearly more HSS activity and therefore a more pronounced HSS maximum. The maxima of the histograms is for 1998 around 400 km/s and for 2003 440 km/s. This high velocity distribution is the basis for defining HSSs in this thesis.

3.2 Definition of HSS

Fast solar wind is a time interval during which the velocity x-component (Earthward) reaches values over 700 km/s. In order to not take into account plasma velocity fluctuations, causing small disturbances in the continuous flow, a fast solar wind period only ends when its velocity component $|V_{gsmx}|$ falls below 600 km/s. This definition is justified by the first panel in Fig. 22, where the green-dashed vertical line denotes the start and the red dashed line the end of the HSS. This notation will also be used in the following plots. Due to different resolutions for different ACE spacecraft instruments, the data from the SWEPAM instrument that provides data averaged over 64 seconds are linearly interpolated (containing the velocity and proton density) for the MAG instrument resolution of 16-sec.

The HSS starting point of 700 km/s is supported by the velocity histograms in Fig. 21: Since the deviation of the Gaussian curve is over 500 km/s but less than 600 km/s during the analyzed years, the decision to take 700 km/s as the starting point and a limit of 600 km/s as the endpoint of the fast solar wind period seems to be a good choice: this ensures that no intermediate or slow velocity wind structures are included. In addition, slow ($|V_{gsmx}| < 700$ km/s) coronal mass ejections (CMEs) having no relation to HSS are thereby excluded from the analysis. This is the definition of the fast solar wind periods used in this thesis.

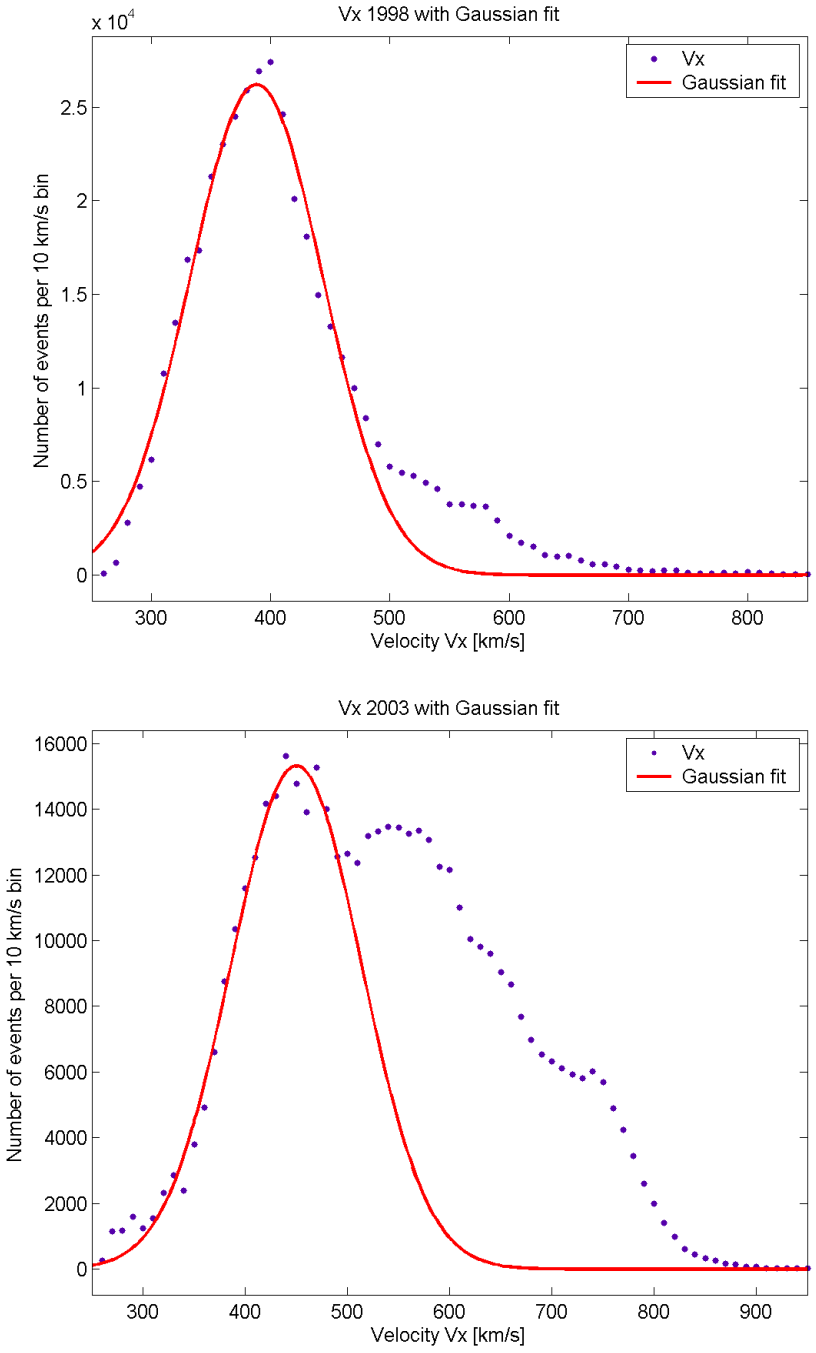

Fig. 21: Velocity distribution in x-direction ($|V_{gsmx}|$) for the years 1998 and 2003

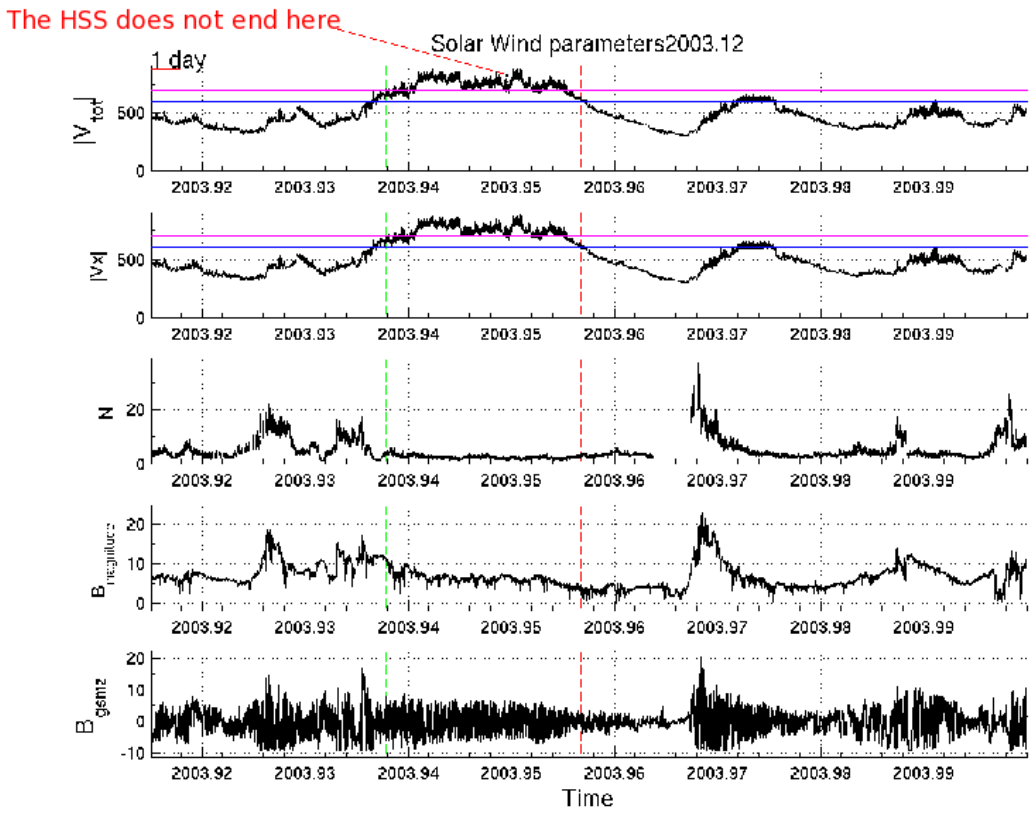

Fig. 22: Solar wind parameters in December 2003. Data taken from the ACE satellite.

An operational criterion to distinguish HSSs from the fast solar wind is a duration of over six hours. This restriction ensures that there is enough time for the loading process in the magnetotail to produce an intense substorm. Further small fluctuations are disregard in order to be able to describe large-scale high-speed stream structures. This HSS definition I call **the two-level definition** throughout the thesis.

3.3 Example HSS, August 1 - 3, 2003 and May 23 - 24, 2002

Two example HSSs are shown in Fig. 23 and Fig. 24. Fig. 23 records strong z-component interplanetary magnetic field (B_{gsmz}) fluctuations on August 1 - 3, 2003 while Fig. 24 shows almost no fluctuations in B_{gsmz} on May 23 - 24, 2002. The total velocity $|V_{tot}| = \sqrt{V_{gsmx}^2 + V_{gsmy}^2 + V_{gsmz}^2}$ is plotted in the first panels of Fig. 23 and Fig. 24. By comparing $|V_{tot}|$ and $|V_{gsmx}|$ (second panel) one can note that they do not differ much. This is due to the direction of the solar wind that blows radially from the Sun and additionally the position of the spacecraft ACE from which the

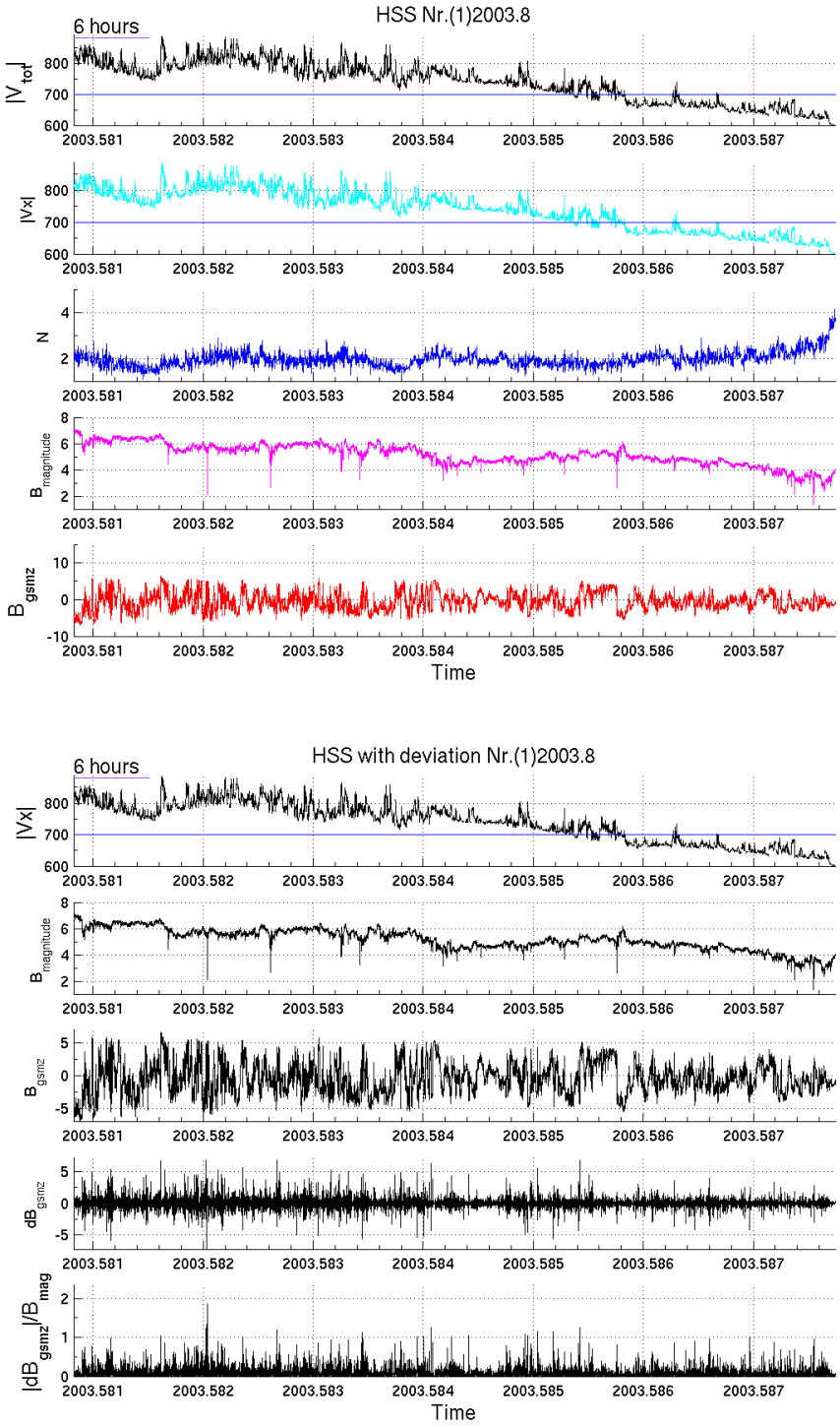

Fig. 23: HSS on Aug 1 at 00:00:33 UT to Aug 3 at 12:38:08 UT, 2003. Strong magnetic field fluctuations can be seen.

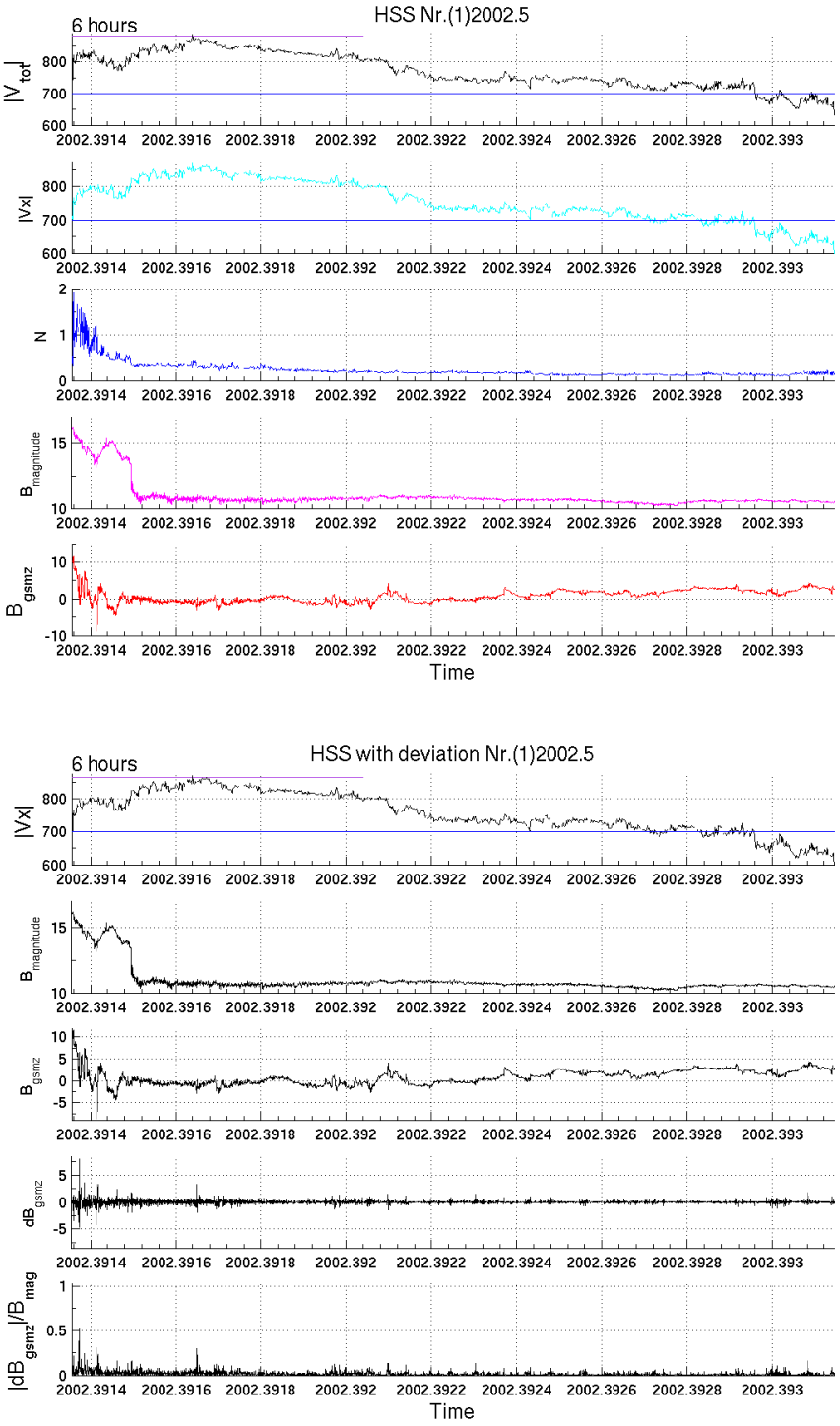

Fig. 24: HSS on May 23 at 20:16:29 UT to May 24 at 11:57:00 UT, 2002 with a calm B_{gsmz} component.

data were used for this plot. ACE is located in the solar wind, on the dayside of the Earth and therefore does not feel the disturbance and deflection of the solar wind caused by the Earth (see Fig. 25). The Pearson correlation coefficient (see definition 1.5) between $|V_{tot}|$ and $|V_{gsmx}|$ is very close to one (0.99989) for the shown period, December 2003.

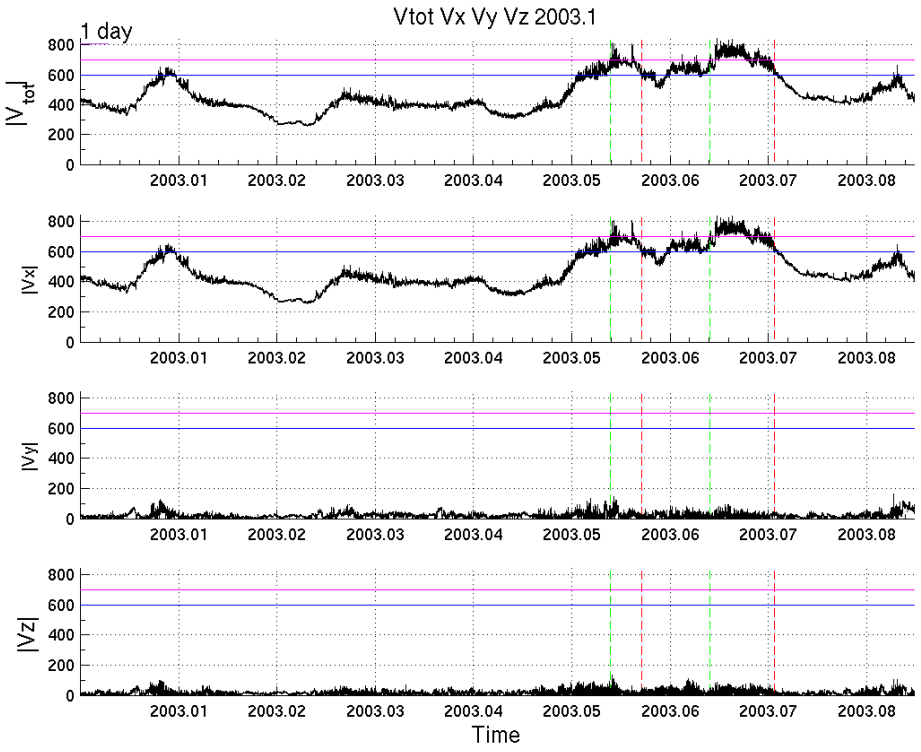

Fig. 25: The total Sun-to-Earth velocity and the velocity components $|V_{gsmx}|$, $|V_{gsmy}|$ and $|V_{gsmz}|$ of the solar wind for January 2003 .

The velocity [km/s] is nearly always slowly decreasing during HSSs, but nearly all events start with a steep rise in velocity (see explanation in Section 1.2.4).

The third panel shows the proton density N [cm^{-3}] which is, as mentioned in Section 1.2, almost equal to the electron density. The solar wind proton density for this example takes values around $2-4\,cm^{-3}$ which is characteristic for HSSs (see table 2). During HSSs the density is usually constant or slightly decreasing, but before the HSS period a clear peak in the density can be found (see Sections 5 and 5.3 for discussion).

The z-component of the interplanetary magnetic field B_{gsmz} [nT] fluctuates roughly between $\pm$ 5 nT. The magnitude of the interplanetary magnetic field $B_{magnitude}$ [nT] has a similar behaviour to the B_{gsmz}. When the proton density increases, the fluctuations in the B_{gsmz} increase simultaneously, since the field lines move together

with the plasma. In order to study the influence of an HSS on the disturbances at Earth, the interplanetary magnetic field needs to include southward periods (when B_{gsmz} has negative values). The reason for the importance of the negative B_{gsmz} is the clearly enhanced efficiency of the energy input through the reconnection process at the Earth magnetopause, which enables substorms to occur (see Section 1.4.4). Large amplitude Alfvén waves in the interplanetary magnetic field, which are observed within HSSs, show enhanced B_{gsmz} fluctuations and are therefore an essential feature of HSSs that can trigger substorms. This insight was already published in 2006 [13]. Alfvén waves, their occurrence and necessity for this research will be considered in a later Section 5.4.

In the lower panels of Fig. 23 and Fig. 24 the magnetic field fluctuations dB_{gsmz} [nT] and the ratio $|dB_{gsmz}|\,/dB_{mag}$ are plotted. One can see that in both examples shown, the fluctuations are higher at the beginning of the HSS than in the later part. This feature will be addressed in Section 5.1.

In order not to consider only one particular HSS, a superposed epoch analysis of an entire year of HSS observations for the years 1998 – 2007 was conducted. Fig. 26 shows the result for the year 2003. This superposed epoch analysis demonstrates the typical features by plotting the median of all HSS at every of the 1000 evenly distributed points in each HSS for the five parameters $|V_{gsmx}|$, the proton density N, B_{gsmz}, $B_{magnitude}$ and the AL index during high-speed streams, where the AL index [nT] is measured at Earth and the other data are taken from the ACE spacecraft.

Because of the different measurement locations the change in AL index follows later than the variation in the $|V_{gsmx}|$. This time-shift of the AL index data with a delay of approximately 40 min. for fast solar wind is not necessary since 40 min. are only a small fraction of the entire HSS duration.

This superposed epoch analysis does not provide information about the HSS durations but rather represents their global behaviour. A slow decrease is seen in the proton density. Here the rapid velocity increase at the beginning of HSSs (green dashed vertical line) become apparent.

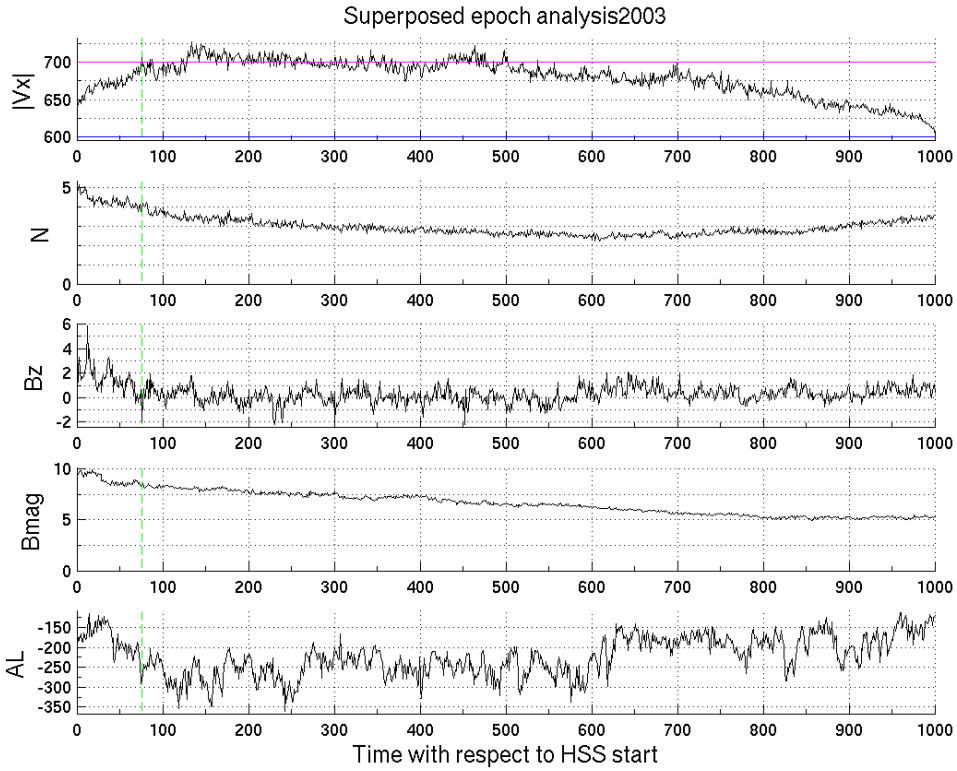

Fig. 26: Superposed epoch analysis for HSSs during the year 2003. The length of every HSS is normalised from 0 to 1000.

3.4 Occurrence of HSS

The dependence of the occurrence of fast solar wind periods and HSSs on their definitions is shown in Fig. 27 and 28. $V_{start/end} = 700\,km/s$ represents the case where the HSS starts and ends when exceeding or falling below the limit of $V_{start/end}$, respectively, where V is the solar wind velocity in the Earthward x-direction in GSM-coordinates measured on the ACE spacecraft (see Section 1.3.2). $V_{start} = 700\,km/s$, $V_{end} = 600\,km/s$ denotes the two-level definition. In these two figures two effects play a role:

- **The number of HSSs can decrease** when using the two-level definition. The operating process is HSS periods (> 6h) in which the velocity $|V_{gsmx}|$ exceeds 700 km/s but suddenly falls to a value between 600 km/s and 700 km/s, and then goes back up to 700 km/s. This variation of fast solar wind can happen due to small plasma fluctuations and is not taken into account by the two-level definition. Instead of two HSSs according to the $V_{start/end} = 700\,km/s$ definition (each exceeding already a duration of 6 h), one only gets one long HSS by using the two-level definition.

- **The number of HSSs can increase** when the two-level definition is used, because an HSS only ends when the velocity falls below 600 km/s. Compared to the $V_{start/end} = 700$ km/s definition where every velocity fluctuation that undershoots 700 km/s forms the end of a fast solar wind structure the two-level definition has a higher probability that the fast solar wind period duration exceeds the 6 hour limit.

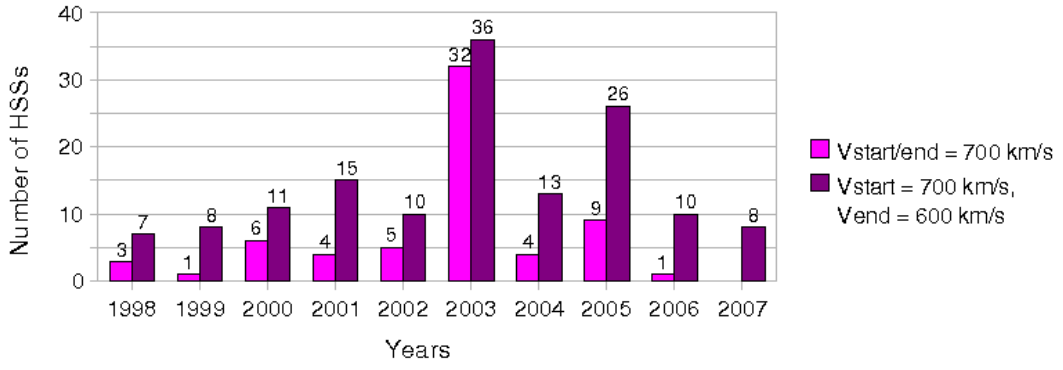

Fig. 27: Number of HSSs in 1998 – 2007 for two different HSS definitions. Note that in the year 2007 the data are only included through June 13, 2007.

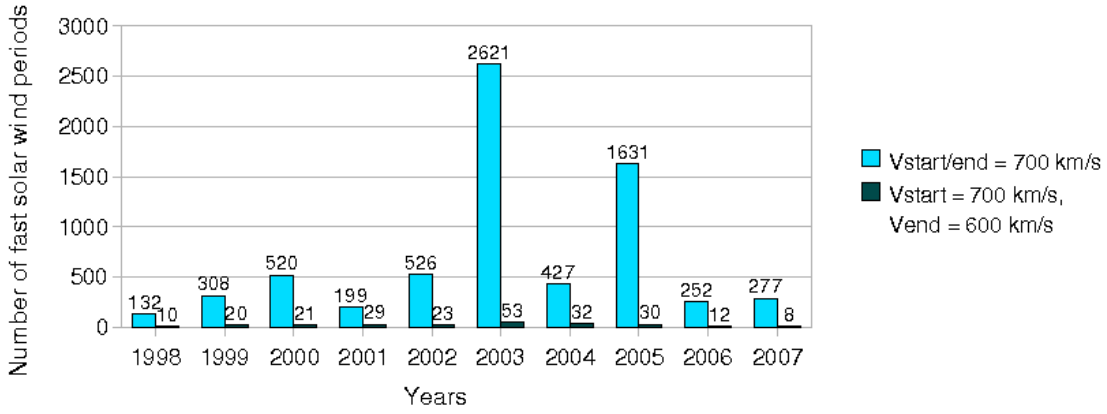

Fig. 28: Number of fast solar wind periods in 1998 – 2007 for two different HSS definitions. Note that in the year 2007 the data is only included through June 13, 2007.

It can be seen from the histograms showing the distribution of HSS from 1998 – 2007 that the second effect plays the key role. Both effects result in an extension of

the HSS duration using the two-level definition instead of the $V_{start/end}$-definition. This can be seen in the duration histogram for the years 1998 – 2006 in Fig. 29. For this illustration the fast solar wind period duration was averaged over every single year using the two-level definition and the $V_{start/end}$-definition, neglecting the 6 hour condition. During these years the fast solar wind durations lasted from 3.7 minutes to 165.7 hours. Typical HSSs have durations of several hours up to one and a half days. The average fast solar wind period durations calculated by using the 700 km/s restriction are additionally multiplied by a factor 10 to display the solar cycle variations, which will be discussed in the following subsection. By looking at the histograms for the fast solar wind period durations in Fig. 28 one can see, that the number of short fast solar wind periods (not HSSs) is very much higher for the $V_{start/end} = 700$ km/s definition than for the two-level definition, which correlates with the higher number of HSSs and the longer durations for the two-level definition.

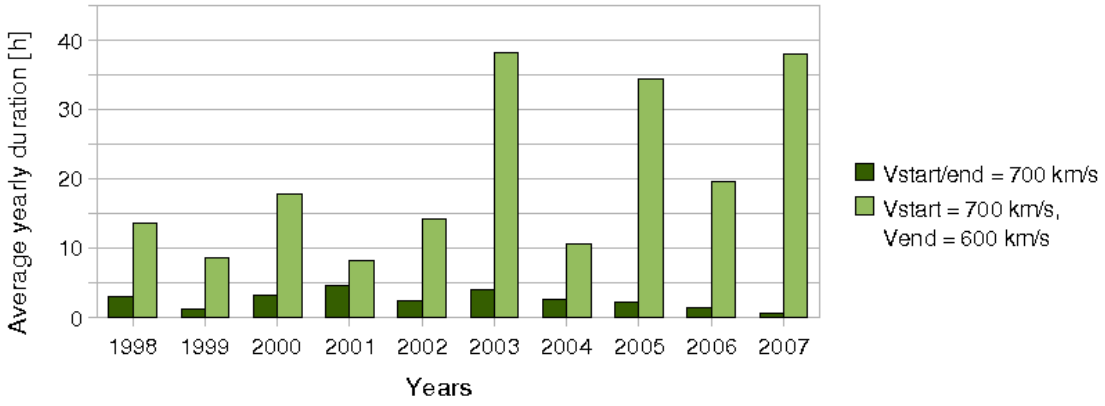

Fig. 29: Average duration of fast solar wind periods over several years. The values for the $V_{start/end} = 700$ km/s definition are multiplied by 10, whereas the number above the bins is the actual average duration. Note: The year 2007 includes only data through June 13, 2007.

Note: One fast solar wind period at the end of 1999 exceeded the end of the year and continued in 2000 when using the two-level definition. This fast solar wind period is taken to be entirely in 2000. The last fast solar wind period in 1999 is therefore neglected in 1999, but added to 2000. The duration of the fast solar wind period is added as well as the part with 600 km/s $< |V_{gsmx}| <$ 700 km/s to the first HSS in 2000, between the beginning of the data and the first HSS, in which the velocity never fell below 600 km/s.

3.4.1 Solar cycle variations

The solar cycle can have an influence on the number of HSSs occurring (see Section 1.4.7). The number of HSSs and the duration of fast solar wind periods during the years 1998 – 2007 have first a small peak around the solar maximum and later, in the declining phase, the peak reaches maximum values (compare Fig. 27, Fig. 28 and Fig. 29). HSSs are more often observed during the declining phase of the solar cycle. This will be explained in the next section. The small peak at the solar activity maximum is due to the complex structure of the HCS during the solar activity maximum.

By taking a look at the overall distribution of the fast solar wind durations (see Fig. 30), one can see the same trend for the median and mean of the duration during the declining phase of the solar cycle: the median and mean value are clearly enhanced. The errorbars show the standard deviation of the duration. They are

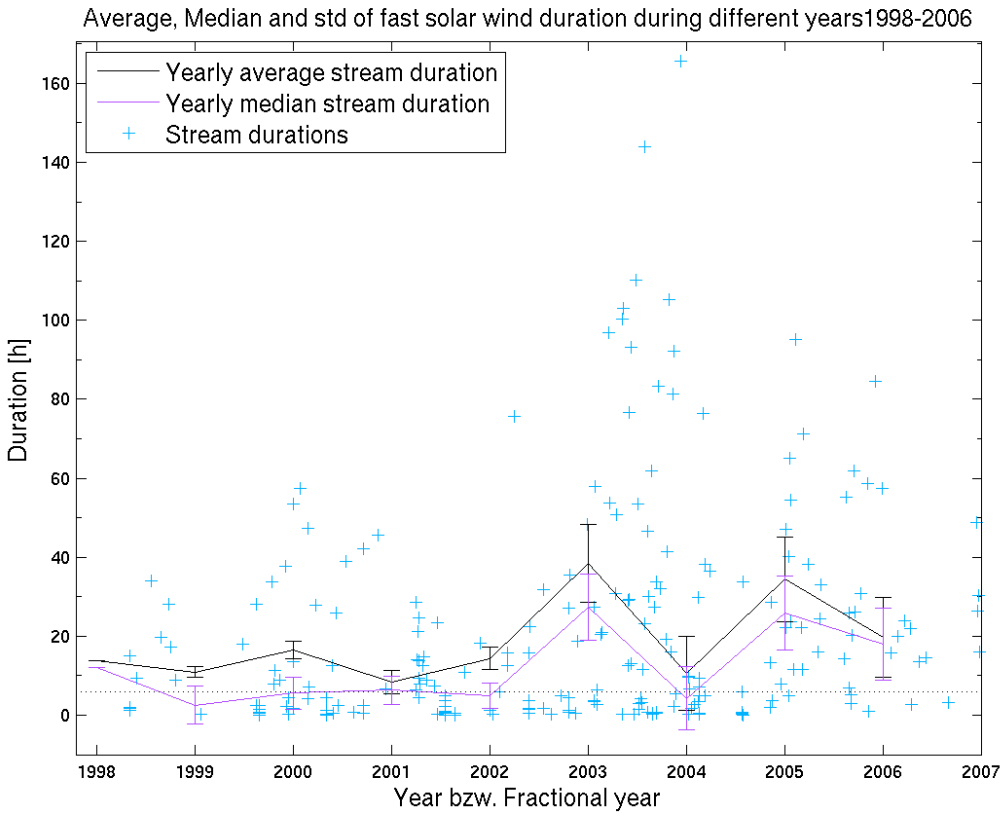

Fig. 30: Mean and median duration together with their standard deviation of fast solar wind periods over several years. The black dotted line is the limit value that separates fast solar wind periods from HSSs.

wider during years with a higher number of HSSs consistently with the declining solar activity, meaning that in these years the data points are further away from the mean duration value. By assessing the duration histograms for different years 1998 – 2006 (Fig. 31), the additional piece of information is made clear, that 2003 is the only year during which HSSs show durations longer than 120 hours. This is what causes the height of the peak in Fig. 29 and Fig. 30. But not only these four HSSs are responsible for a higher yearly average duration. Fig. 31 shows a clear maximum peak in 2003 for nearly every duration bin.

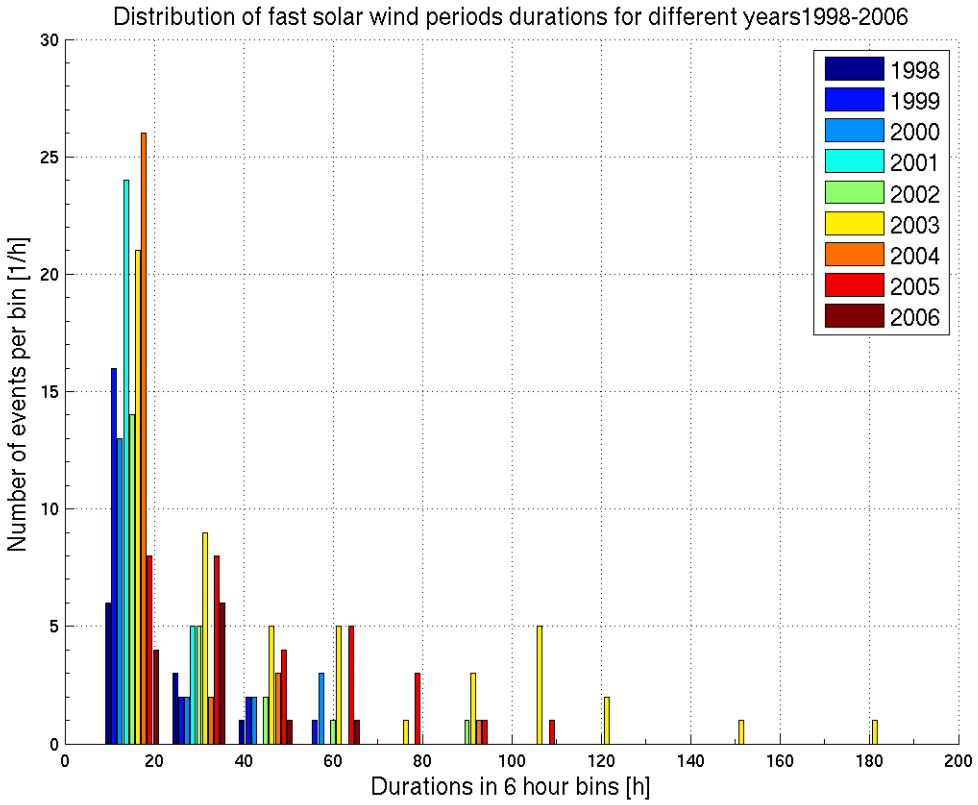

Fig. 31: Fast solar wind period duration histogram over the years 1998 – 2006.

The reason why long lasting HSSs are much more common during the declining phase of the solar cycle is probably the long-lived coronal holes during the late declining phase and the solar minimum.

The velocity $|V_{gsmx}|$ distribution (Fig. 32) shows a tendency to be broader during the decreasing solar activity phase and the solar minimum (darker color) than during the other phases in the years 1998 – 2006. This leads to the presumption that long-lived coronal holes eject faster solar wind streams. Especially interesting is the year 2003 which features very high velocity HSSs. Additionally remarkable is that the number of slow solar wind periods is approximately the same for all years, except for 2003.

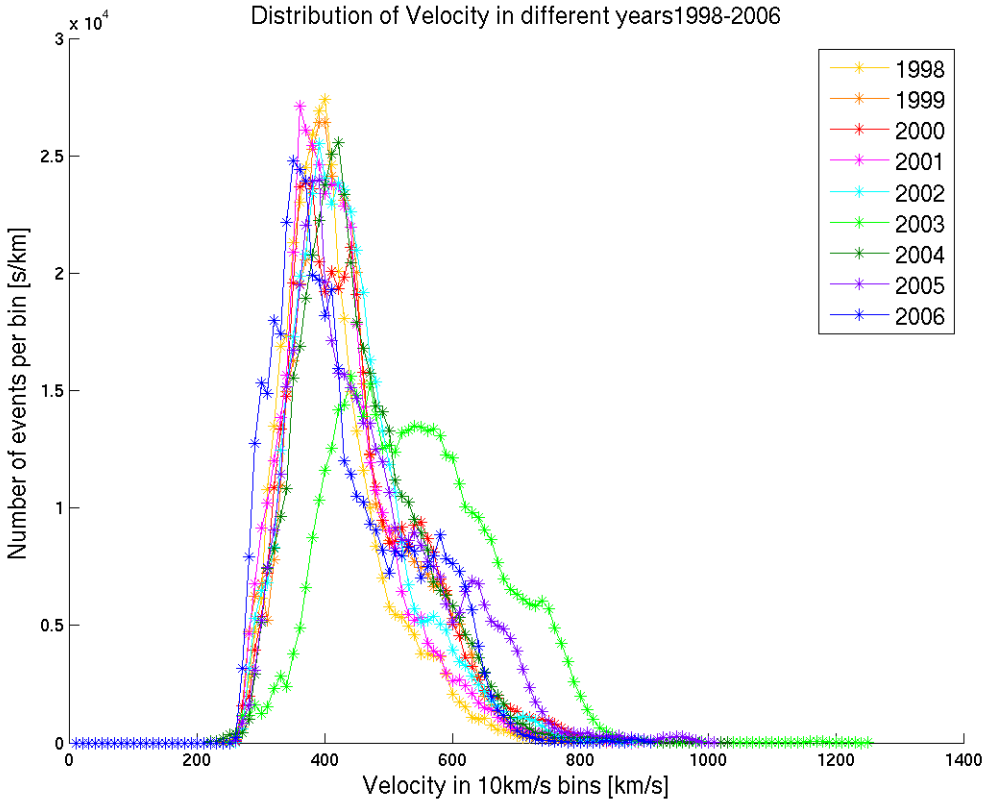

Fig. 32: Velocity distribution during the years 1998 – 2006.

3.4.2 Solar rotation variations and coronal holes

At this point it is important to remind that not all HSSs can be caught by ACE - many structures travel from the Sun outward without reaching the spacecraft. This fact is important to remember especially for the Figures 33 - 36.

The rotation of the Sun affects not only the structure of the heliospheric current sheet as seen in Section 1.2.2, but also the solar wind parameters measured on a satellite, ACE for instance. Since HSSs originate in open field lines of the solar

corona, they co-rotate with the synodic 27-day rotation period of the Sun (Fig. 33 - Fig. 36). The data are of certain interest especially around 2007 because solar cycle 23 just reached its minimum on January 4, 2008, meaning that the solar cycle 24 has started.

Yellow stripes in Fig. 33 – 36 are regions were magnetic clouds have been spotted. Their boundary times are taken from the list of magnetic clouds that was produced using the magnetic field model of Lepping et al. in 1990 [14], available on the NASA webpage $http://lepmfi.gsfc.nasa.gov/mfi/mag\_cloud\_pub1.html$.
The data for this analysis are from the WIND and IMP-8 spacecraft. I make use of it in order to distinguish between HSSs and magnetic clouds. The green and red vertically dashed lines represent the start and end of HSSs respectively. The red stars are drawn with a period of 27 days.

If once more the influence of the solar cycle on the occurrence of HSSs is considered, one can draw some conclusions by looking at the correlation between HSSs and the solar rotation in Fig. 33 (increasing solar activity) and Fig. 34 (decreasing solar activity) which is illustrated for all the considered years in Fig. 37. Shown is the number of correlating HSSs relative to the total number of HSSs for every year separately. To get the percentage of correlation the red stars were counted that can be clearly associated with an HSS, meaning that the star is in between an HSS interval or very close to it and no magnetic cloud is superposed. This number then is devided by the total number of HSSs. There is a good correlation between the solar rotation and HSSs during a solar activity minimum and a decreasing solar cycle phase, while during a solar activity maximum and a increasing solar activity a weak correlation can be found for the solar cycle 23. During the latter times clear variations in the solar wind velocity can be seen, but it is difficult to find the 27-day solar rotation period, since there are many small unclear velocity peaks that do not reach the duration of 6 h and a velocity of 700 km/s that would give rise to an HSS. During some years of declining solar activity, for example in 2007, several coronal holes lasted slightly longer than one solar rotation, but were then replaced by others in the middle of the year, after which a new 27 day rhythm started.

From these general statements and the assumption that most HSSs originate in coronal holes it can be concluded that the lifetimes of coronal holes are shorter ($<$ 27 days) during a solar activity maximum, so that one cannot observe the effects of one coronal hole again after a full rotation of the Sun. A shorter lifetime of the coronal holes on the other hand also accounts for a smaller observed number of HSSs around a solar activity maximum, since they hardly exceed the 6 h limit.

Coronal holes are mainly in the polar region and extend towards the equator around the solar minimum. During a solar activity increase smaller coronal holes emerge near the poles and migrate toward the solar equator. At solar maximum coronal holes are found near the equator. This means that more solar wind velocity variations are observed during the solar maximum times because of an enhanced probability of the flow from the coronal hole of reaching the Earth and an unsteadiness of the holes and their position. This supports the observation of higher velocity fluctuations in Fig. 33.

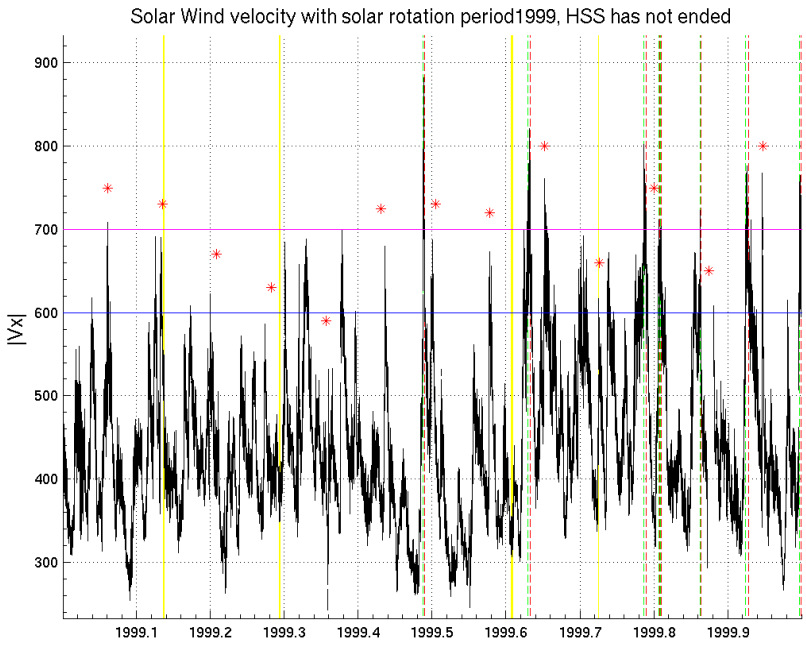

Fig. 33: HSSs velocity $|V_{gsmx}|$ in relation to the solar rotation period in 1999 (increasing solar cycle)

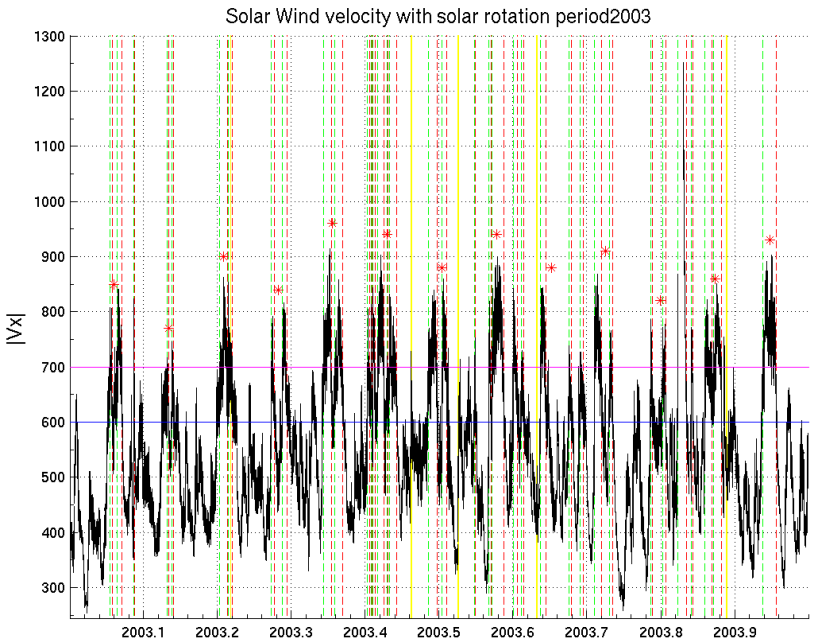

Fig. 34: HSSs velocity $|V_{gsmx}|$ in relation to the solar rotation period in 2003 (decreasing solar cycle)

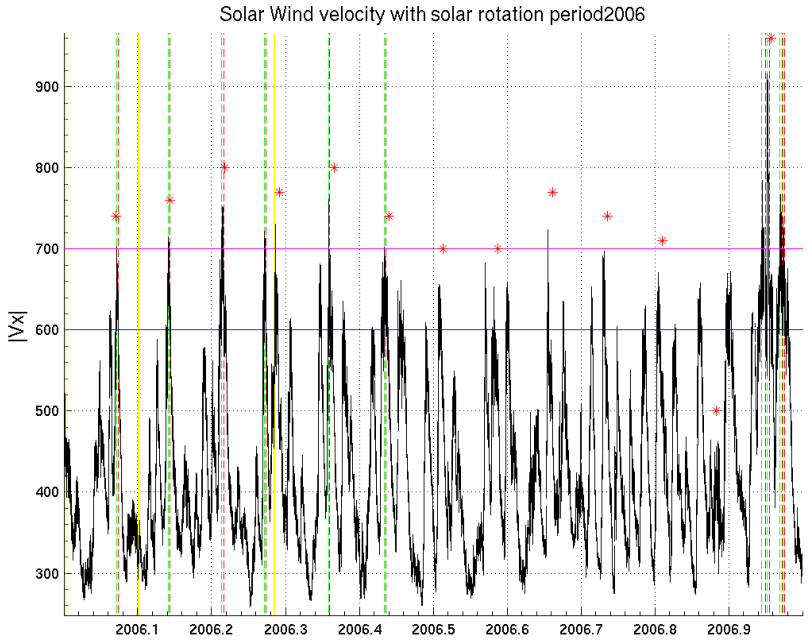

Fig. 35: HSSs velocity $|V_{gsmx}|$ in relation to the solar rotation period in 2006

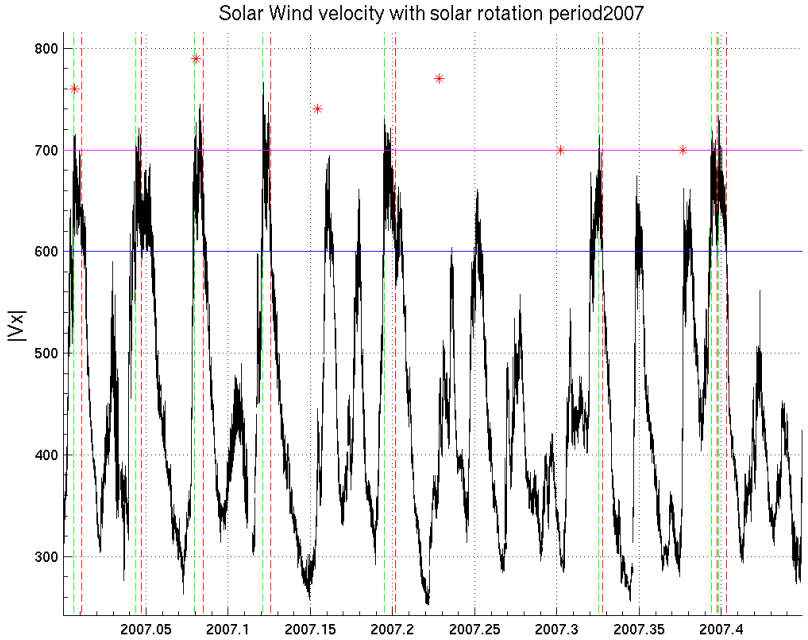

Fig. 36: HSSs velocity $|V_{gsmx}|$ in relation to the solar rotation period in 2007. The data set of this year ends on June 13, 2007.

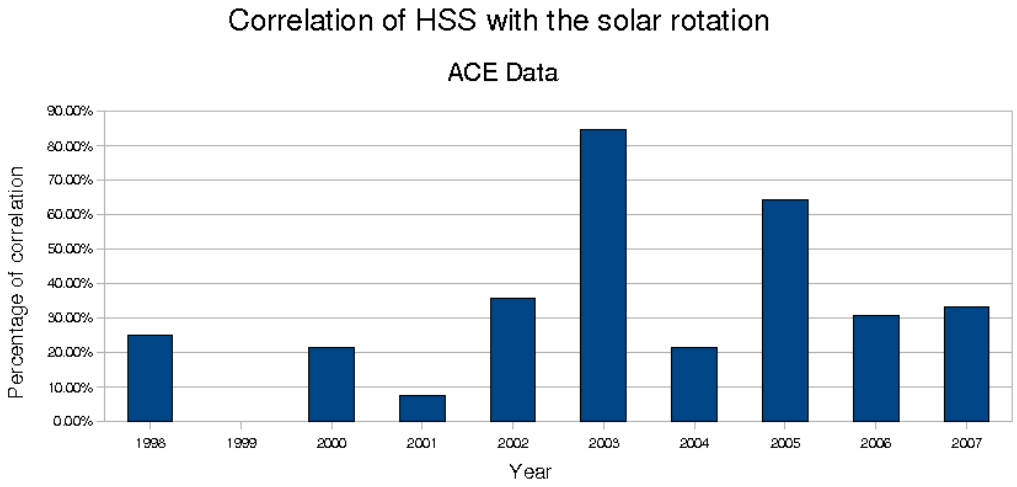

Fig. 37: Correlation of the HSS occurrence and the solar rotation period for the years 1998 – 2007. Note: The dependence on the definition of HSS does not play a relevant role for this graphic.

From the lower speeds during the increasing and the solar maximum activity times as seen in the previous subsection, can be concluded that there is a lower coronal hole activity during these times. This correlates with the shorter lifetime. From the knowledge that the polar coronal holes show a much higher extent during a solar minimum, during which the HSS velocities are higher (as seen in Fig. 32), one can assume that velocities originating from small coronal holes are lower than the ones coming from coronal holes covering large areas.

These results are at least true for the solar cycle 23, but the same results are also expected for other solar cycles. By looking at scientific articles about the correlation between HSSs and coronal holes, a perfect support is found for the previous assumption: Fainshtein and Rudenko (2004) [7] stated that on average the area of short-lived coronal holes is smaller than that of long lived holes. One year later Jun Zhang, Woch and Solanki [23] confirmed the observation of small-scale coronal holes at solar maximum and large-scale polar coronal holes at solar minimum and added that solar wind streams emanating from small-scale holes generally had lower velocities of 400 to 600 km/s compared to the polar hole stream velocities of 700 to 800 km/s. They further made a note that Ulysses encountered several short-duration coronal-hole streams emanating from small-scale coronal holes emerging at mid and low latitudes during the maximum activity phase of cycle 23, in 2000.

Coronal holes last for weeks, months and, exceptionally, even years. Long lasting structures are predominantly found during a solar activity minimum or a declining solar activity. Then their size is much larger, covering sometimes as much as a quarter of the surface of the Sun. This means that during a solar activity decrease the correlation between the solar rotation and the occurrence of HSSs is expected to

be much better, while during a solar maximum coronal holes often last for a shorter time period and therefore a smaller number of HSS is detected. But it is important to keep in mind, that for both polar coronal hole streams the speed does not need to be constant over the coronal hole lifetime. Thus a long-lasting coronal hole does not necessarily create one long-lasting HSS. Observations of coronal hole regions can be used to predict the solar wind speed at the Earth. There are already models available e.g. by S. Robbins at al. [16]. Their accuracy is within 10% of the solar wind speed measurements at best.

4 Interaction of the solar wind with the magnetosphere

Substorms are thought to be closely relateted to HSSs [20]. The most intense and frequent substorms are observed during the same solar phase as HSSs. The association of repetitive substorms with large amplitude Alfvén interplanetary magnetic field fluctuations during HSSs has been reported before (e.g. Lee et al. 2006 [13]). The term repetitive substorms represents periodic substorms that occur every 1 – 4 hours and last similar to HSS 1 – 6 days. The reason for this relation is possibly the repetitive turnings of the interplanetary magnetic field during HSSs that gives rise to reconnection at the magnetopause of the Earth and thus could be identified as a substorm trigger. It has become apparent that repetitive substorms occur, regardless of the solar cycle phase, whenever HSSs with large amplitude Alfvén waves interact with the magnetosphere of the Earth [13].

When studying the solar wind parameters $|V_{gsmx}|$, N, B_{gsmz} and the westward electrojet index AL, one can find that whenever $|V_{gsmx}|$ strongly increases or B_{gsmz} strongly decreases, the AL index decreases rapidly. In addition the AL index during substorm times is known to be enhanced (Fig. 26). Therefore a histogram of the AL index is plotted during HSS periods and slow solar wind as well as for all data during the years 1998 – 2007 (shown is the year 2003 in Fig. 38). Note that the number of events is normalised to the total number of HSSs and slow solar wind periods respectively. It is obvious from these plots that the AL index is generally enhanced during HSSs, meaning smaller than -200 nT. All analyzed years support the association of HSSs with substorms. A glance over the monthly plot for instance in September 2003 Fig. 39 shows an enhanced AL index particularly at the beginning of the HSS. Interesting is the fact, that the rapid decrease in the AL index starts in some events together with the increase in fluctuations in the interplanetary magnetic field and sometimes it only falls to lower values simultaneously with the delayed velocity increase as described in Section 5. Also small scale fluctuations during one HSS, as shown in Fig. 40, cannot be directly related to the velocity $|V_{gsmx}|$ nor to the magnetic field B_{gsmz}. Various complicated relations between $|V_{gsmx}|$, B_{gsmz} and AL have been found (e.g. [19]). The correlation seems to depend on the event and the solar cycle phase.

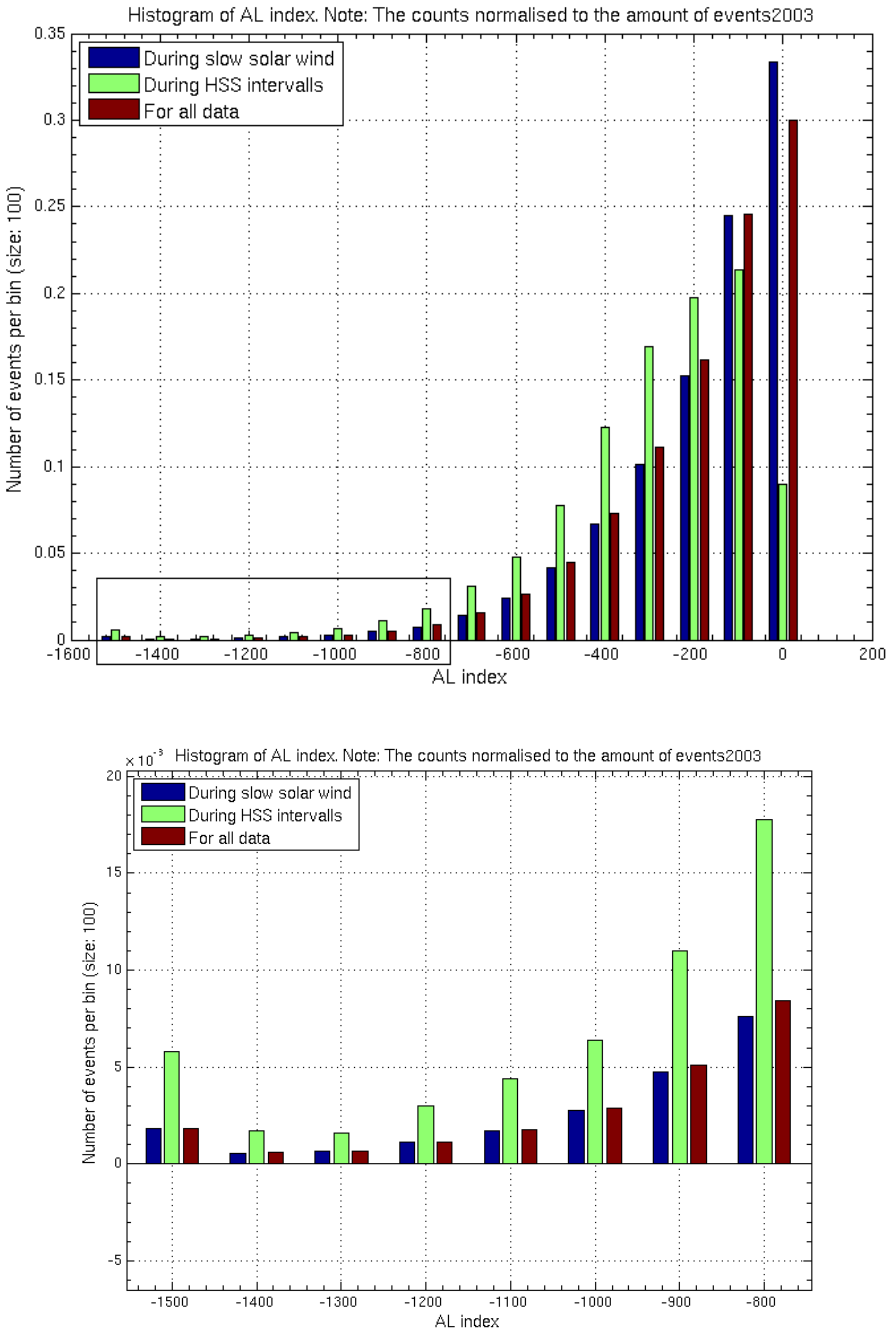

Fig. 38: First panel: AL index histogram for HSSs, slow solar wind periods and all data in 2003. The count in each bin are normalised by the total number of data points for each of the three characteristics separately. Second panel: The rectangle from the upper panel zoomed in.

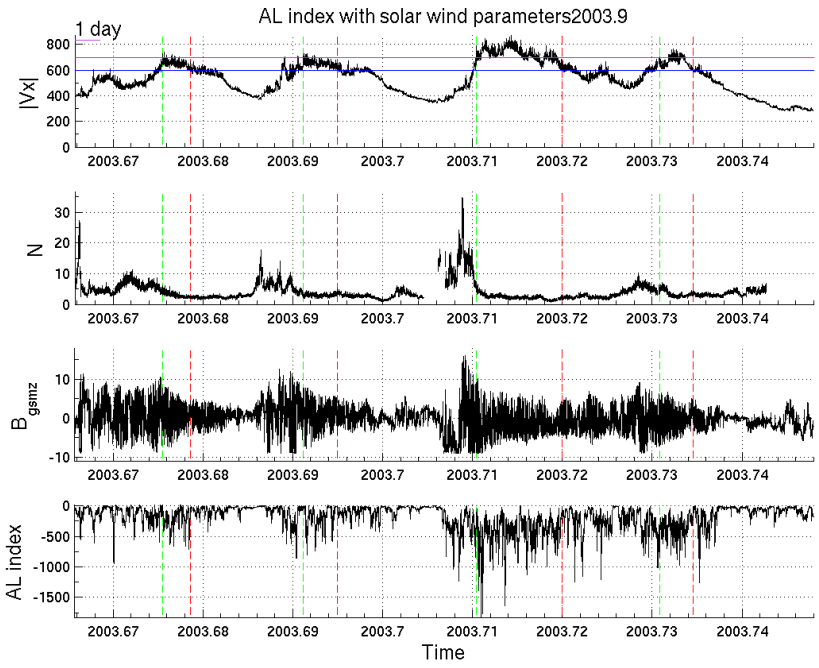

Fig. 39: AL index with solar wind parameters for the entire month Sept 2003

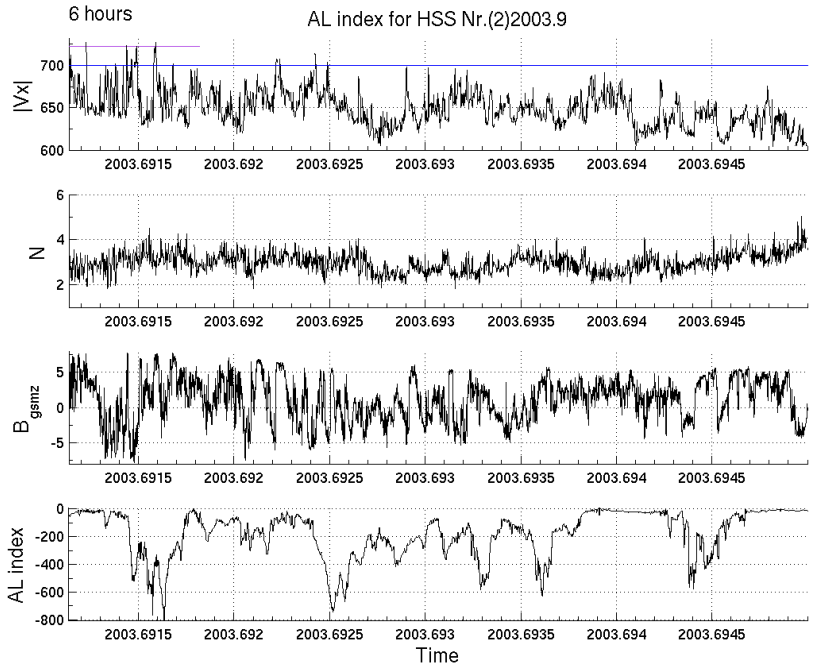

Fig. 40: AL index with solar wind parameters during the HSS on Sept 10, 2003, at 06:20:59 UT until Sept 11, 2003 at 16:11:54 UT

The question why the AL index is enhanced during HSS periods can be answered by considering:

1. Enhanced magnetic field fluctuations at the beginning of each HSS
2. Occurrence of Alfvén waves during HSS periods

By considering again the superposed epoch analysis plot Fig. 26, a more negative AL index can be spotted especially at the beginning of HSSs. This correlates with the observations of enhanced magnetic field fluctuations in the first 10 - 15% of the duration of each HSS (see Section 5.1.1). Since southward turnings of the interplanetary magnetic B_{gsmz} are a condition for reconnection at the magnetopause to happen, substorms are more probable during HSSs and thus is the AL index more negative. One can even connect the second previously mentioned item to this chain. Alfvén waves show enhanced fluctuations in the B_{gsmz} component and hence have a connection to interplanetary magnetic field turnings.

5 Typical HSS features

5.1 Interplanetary field fluctuations during HSSs

I start this discussion with a superposed epoch analysis Fig. 41. It shows the large-scale behaviour of the five parameters $|V_{gsmx}|$, B_{gsmz}, the fluctuations of the $|V_{gsmx}|$ and B_{gsmz}, denoted as $|dV_{gsmx}|$, dB_{gsmz} and the AL index during HSSs. A clear decrease in $|dV_{gsmx}|$ and dB_{gsmz} during an HSS can be seen. It raises the question of if the fluctuations dV_{gsmx} and dB_{gsmz} are higher at the beginning than in the end of HSSs. To examine this possible property one needs to take a closer look at the individual HSSs.

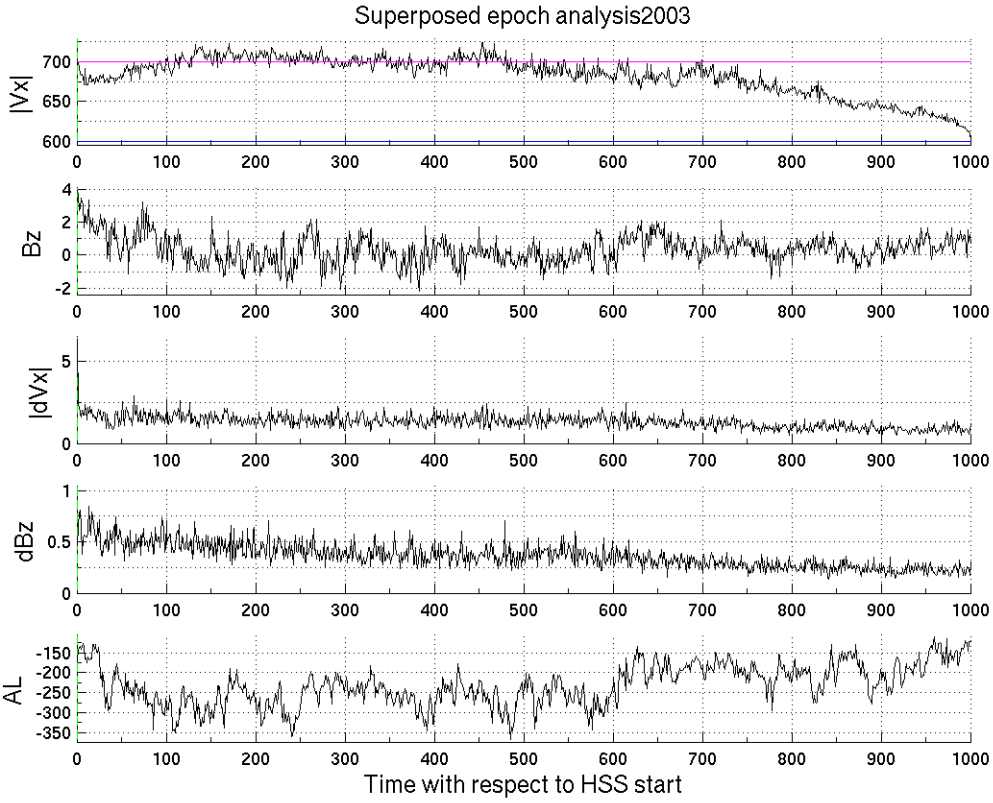

Fig. 41: Superposed epoch analysis for the year 2003. The length of every HSS is normalised from 0 to 1000.

5.1.1 Magnetic field fluctuation during HSS

By looking at the solar wind parameters $|V_{tot}|$, $|V_{gsmx}|$, N, $B_{magnitude}$ and B_{gsmz} during HSSs one can presume an increased fluctuation dB at each beginning of an HSS period. The field fluctuations dB are calculated by

$$dB(i) = B_{gsmz}(i+1) - B_{gsmz}(i) \tag{18}$$

For now the direction of the fluctuations is unimportant. Only the absolute value of dB_{gsmz} is considered. Fig. 42 shows evidence that in the first 10 - 15% of every HSS duration, median(dB) is higher than the value obtained for the entire HSS. In Fig. 42 the difference of median(dB_{gsmz}) calculated for the first 10% of the duration and the entire duration of the fast solar wind period is plotted. The blue vertical line denotes the boundary between fast solar wind periods that last less than 6 h and HSSs.

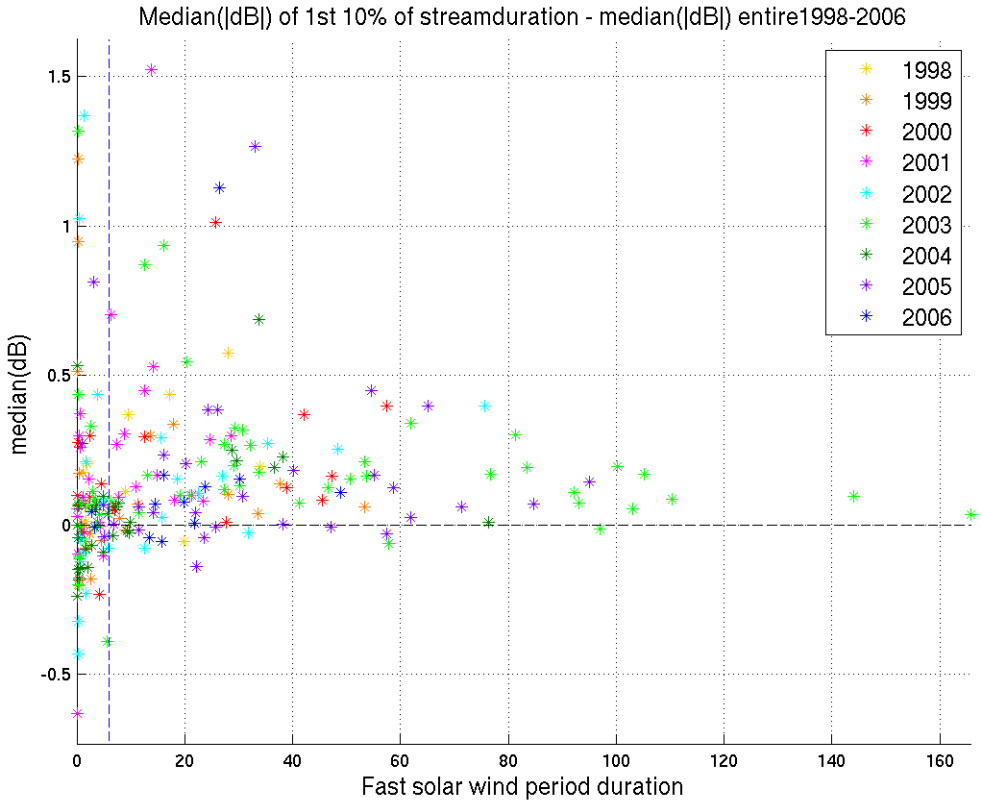

Fig. 42: Median(dB_{gsmz}) versus the fast solar wind duration for the years 1998 – 2006. Median(dB_{gsmz}) is clearly enhanced during the first 10 - 15% of the HSS duration - independent off their total duration.

The solar wind periods lasting less than 6 h are less predictable in their magnetic fluctuations and they are dropped from this discussion because they are not HSSs. Different colors refer to different years. With the Fig. 42 the hypothesis of higher fluctuations in the magnetic field z-component at the very beginning of an HSS is strongly supported. Additionally it enable to tell about variations based on the solar cycle. It seems that most of the HSSs support this hypothesis, but during the declining solar cycle there are a few inappropriate behaviours. It can now either be that since during the declining phase of the solar cycle there are more HSSs and thus the chance of being inappropriate is higher for this phase or it can also be a conclusion that HSS are much more irregular in their behaviour during a solar activity decrease. This will stay an open question as long as no other solar cycles are taken into account to compare and thus no good statistics over time scales of several solar cycles.

Let us take a look at a case (see Fig. 42) where the median of the magnetic field fluctuations in the first 10% of the HSS duration are smaller than the one from the entire HSS interval. For instance the year 2003 Fig. 43. Now plotted is the value of median(dB_{gsmz}) for the entire fast solar wind period in black and median(dB_{gsmz}) only calculated using the first 10% or 15% of the fast solar wind period (green stars). Two HSSs seem to misbehave: With a fast solar wind period duration of ∼58 h and ∼97 h. The result is the same for 10% and 15% of the HSS durations. In a next step the HSSs are closer inspected by looking at their solar wind parameters in Fig. 44. There is a short time interval of about 1 h 7 min. shown before the HSS starts (green vertical line) to see its time development.

As described in a previous section the $|V_{gsmx}|$ component and thus also the $|V_{tot}|$ characteristically rise rapidly at the beginning of an HSS but decreases slowly. This feature is not taken into account in the two-level definition. In reality the upper two HSSs start later in time, at about 2003.0646 (in the upper panel) and 2003.2034 (in the lower panel), respectively. By correcting their starting time a stronger magnetic field fluctuation region at the new beginning of the HSS is found.

What do magnetic field fluctuations tell us about the nature of HSSs? They are thought to be a result of the stream interface that occurs shortly before an HSS starts, for which period a strongly fluctuating magnetic field is characteristic. Thus one would still see the effects of the stream interface (see Section 5.3) at the beginning of the HSS. The fact that the magnetic field fluctuations are enhanced at the beginning of HSSs is also in correlation with the Alfvén waves that can be observed during HSSs. But as mentioned before, strong magnetic fluctuations do not directly imply the presence of Alfvén waves.

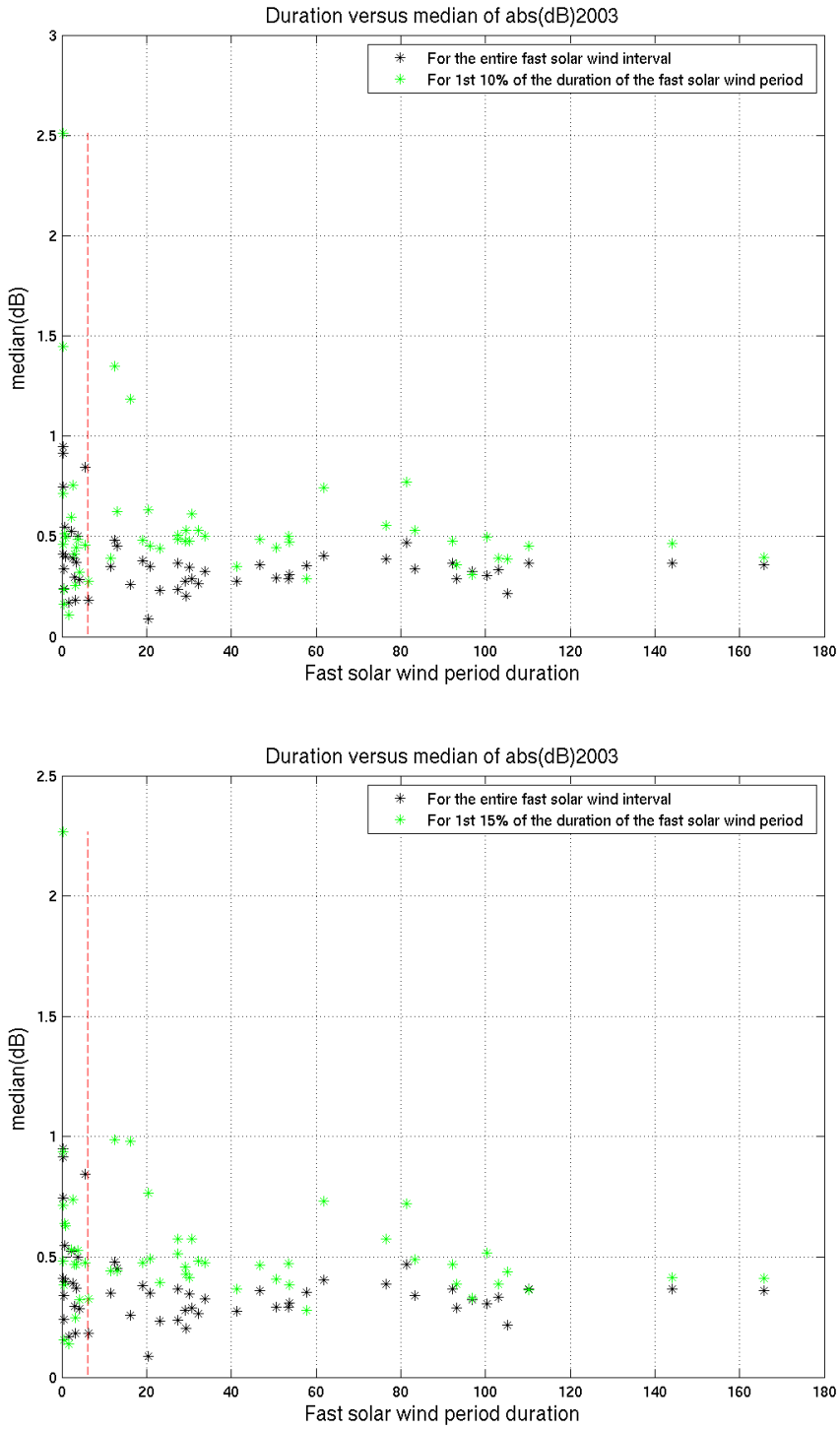

Fig. 43: Median(dB_{gsmz}) from the first 10% (upper panel) and 15% (lower panel) of the fast solar wind and the entire fast solar wind interval duration in the year 2003.

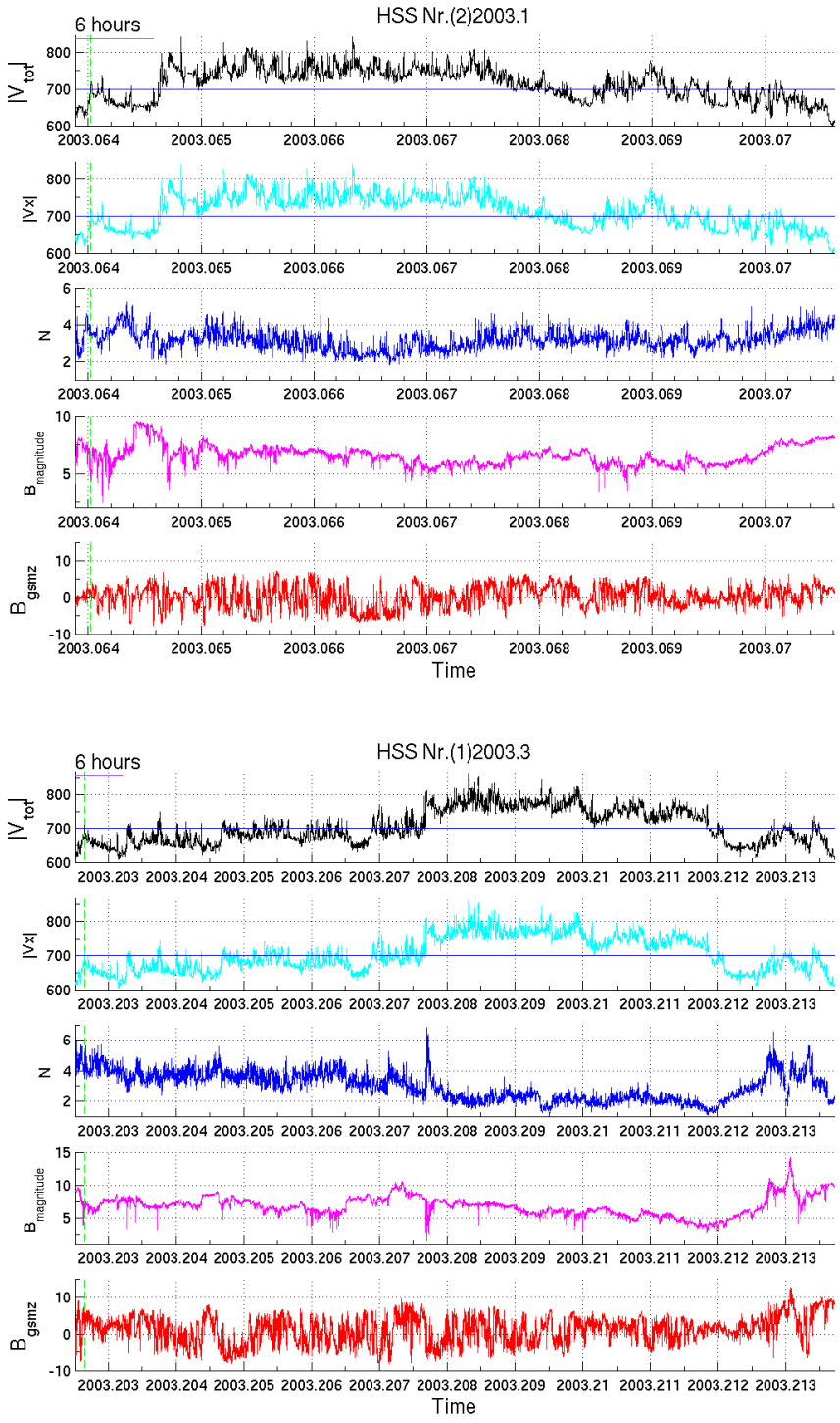

Fig. 44: Examples of two HSSs with a suboptimal start definition on Jan 24 at 08:48:10 UT until Jan 26 at 18:38:34 UT, 2003 and Mar 15 at 23:16:03 UT until Mar 20 at 00:13:39 UT, 2003. Thus durations are 58 h and 97 h, respectively.

5.1.2 Velocity fluctuation during HSSs

Considering the velocity variations during an HSS the same phenomenon was found as for magnetic field fluctuations. The first 10 - 15% of the entire HSS duration contain more velocity variations than the total HSS period. This result is illustrated in Fig. 45. It is a new result that cannot be explained with the presence of Alfvén waves at the beginning of HSSs. The blue vertical line shows the border between fast solar wind with durations of less than 6 h and HSSs.

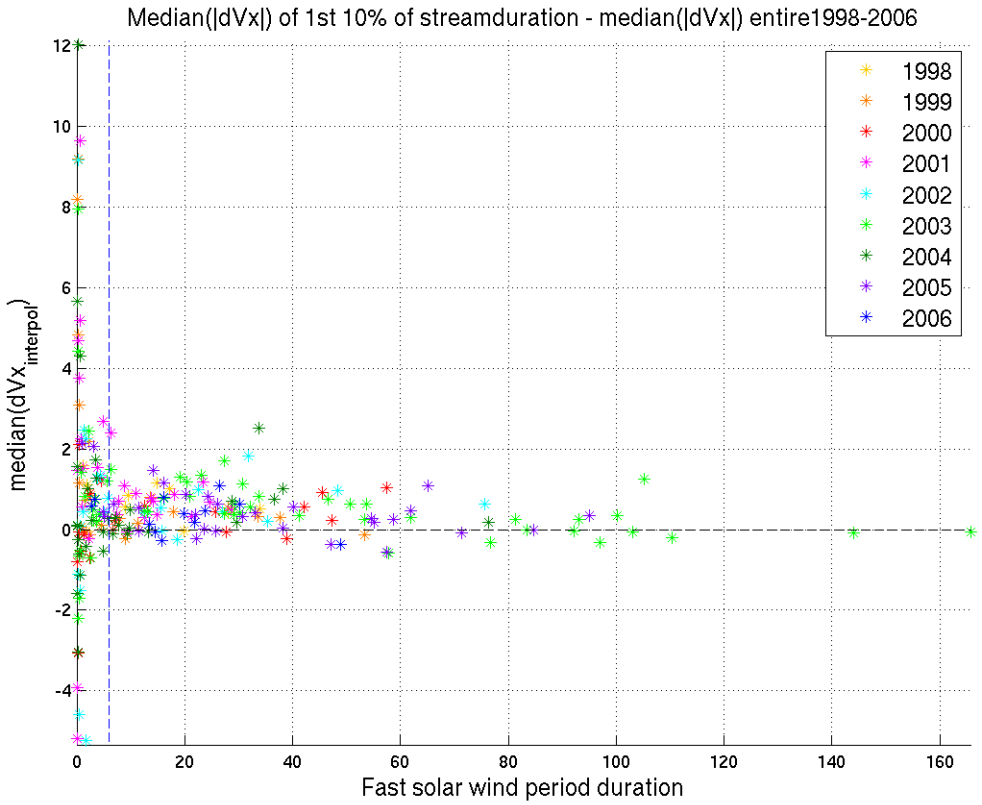

Fig. 45: Median(dV_{gsmx}) versus the fast solar wind duration for the years 1998 – 2006. Median(dV_{gsmx}) is clearly enhanced during the first 10% of the HSS duration - independent off their total duration.

It can be once again seen by going into details of the year 2003 (Fig. 46), that the HSS with the duration of ∼58 h and the one with ∼97 h do not follow the fluctuation hypothesis - as can be expected by using the same reason as given for the magnetic field fluctuations. There are further the streams with durations of about 110 h and

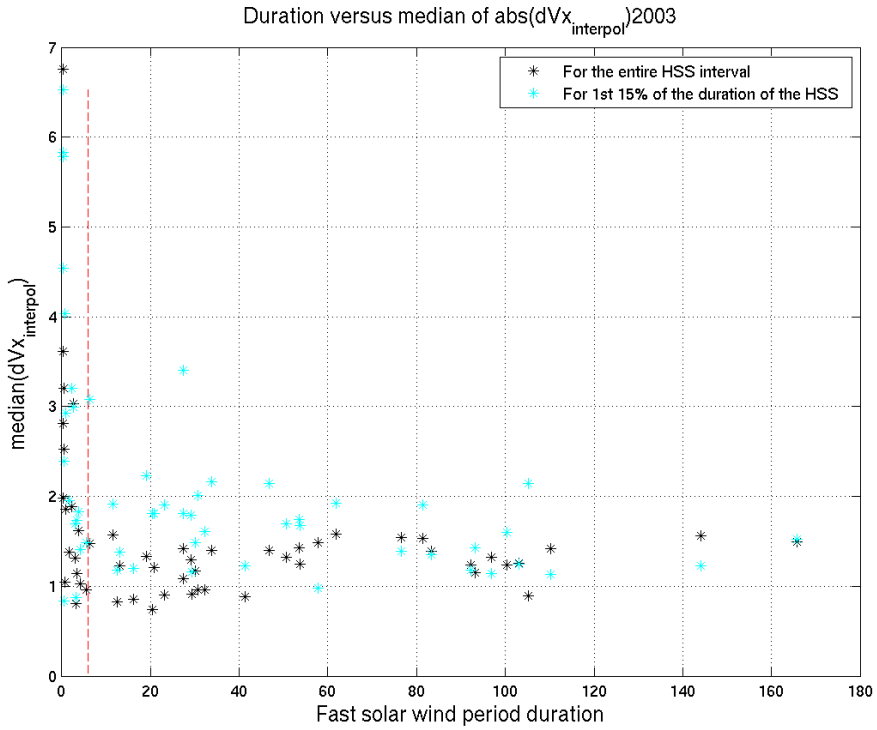

Fig. 46: Examples for the HSS period with a suboptimal start definition and an impure HSS structure.

144 h, which seem to behave differently than claimed. By looking at Fig. 47 it can be noticed that they show in no way a typical HSS structure and presumably are overlapping with a CME structure that arrived at the satellite at the same point in time. The bumps in the proton density and also magnitude of the magnetic field are indications for an impure HSS structure. Especially in the second plot of Fig. 47 this bump is clearly accompanied by a typical CME S-form structure in the interplanetary B_{gsmz} around a fractional time of 2003.575. In the first plot the HSS covering CME structure can be found around 2003.489. Eventhough this CME characteristic might not be in the first 15% of the entire HSS duration, it shows that there is something else than a typical HSS structure.

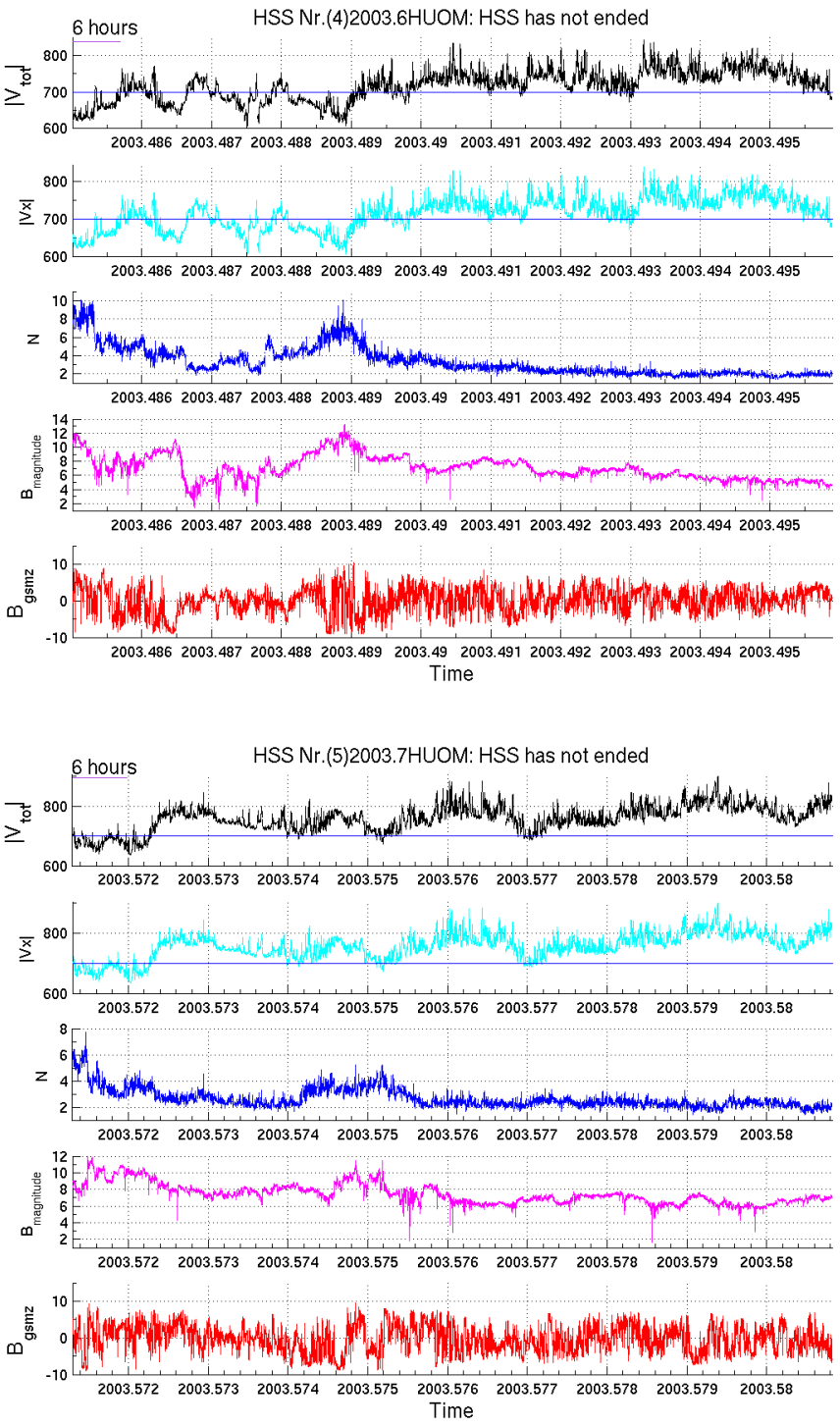

Fig. 47: Examples for HSSs on Jun 27 at 00:38:46 UT until Jun 30 at 23:59:49 UT, 2003, and on Jul 28 at 12:35:29 UT until Jul 31 at 23:59:45 UT, 2003, with an impure HSS structure. Thus durations are about 110 h and 144 h respectively. (The plots do not show the entire HSS period, they would continue in the next month)

5.2 HSS and CIRs

Considering the Parker spiral and the compression between the fast solar wind overtaking the slow solar wind, a steepening in the density is expected to take place every time a sector boundary of the heliospheric current sheet is crossed. This plasma compression occurs slightly before the velocity peak, as was mentioned also in Section 1.2.4 and 1.2.3. It can be concluded that the sector boundary crossings are responsible for the stream interfaces whose typical features will be discussed in the next subsection. The delayed increase in velocity can be explained by looking at the CIRs, where a fast stream interacts with a slow one. The density increase starts before the speed increase because of a compressed solar wind ahead of the fast solar wind (see Fig. 4). The magnetic field variations behave in the same way as the density due to the frozen-in condition. The time interval between the plasma compression at the stream interface and the increase in velocity is in the considered dataset $1-5$ days.

CIRs are very important because of their enhanced field fluctuations within the compressed plasma which may cause scattering and the transport of energetic particles through the heliosphere. CIRs seem to explain some of the structures of HSSs. But it is still not clear how much they are responsible for the generation of HSSs.

5.3 Stream interfaces

Stream interface is an often used term to identify the sharp density drop before the start of the HSS. It is believed that the stream interface marks the boundary within a CIR separating the slow and dense solar wind from the plasma which was originally faster and more tenuous. CIRs are tilted in the same sense as the heliospheric current sheet, because both arise from the same geometry back at the Sun [1].

In the plot (Fig. 48) one can clearly see the stream interface start. Only after the stream interface has passed the satellite the fast solar wind is finally observed, reaching velocities higher than 700 km/s. The CIR boundaries become sharp discontinuities due to the nonlinear evolution in the interplanetary space further out from the Sun than at 1 AU [1].

As noticed by Belcher and Davis (1971) [3] the variability of the magnetic field direction increases at the stream interface as well as the presence of Alfvén waves in the fast wind (Fig. 48). This fact gives the possibility to distinguish between HSS and CMEs as can be seen in the following section. But not all fast solar wind structures at 1 AU show a sharp stream interface and not all stream interfaces result in an HSS, which keeps the relation between CIRs and HSSs still under discussion.

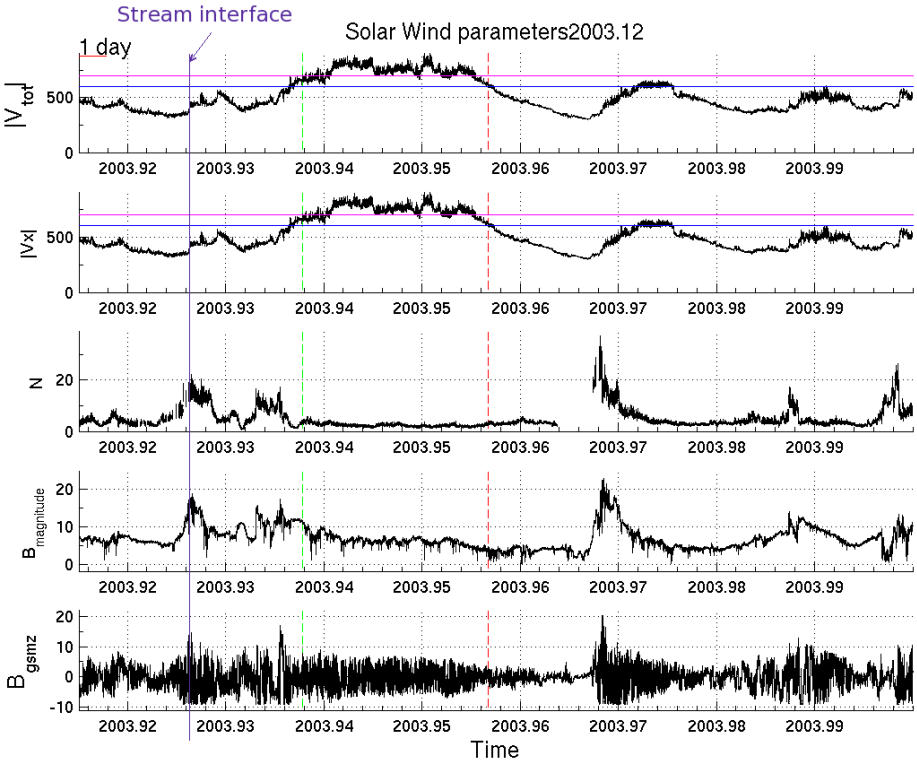

Fig. 48: Stream interface in December 2003 prior to the HSS (start of HSS is the green dashed line).

In the year 2003 31 clear stream interfaces were found that could be associated with an HSS. Five HSSs were difficult to allocate to one distinct stream interface. Together with the stream interface not only a higher fluctuating magnetic field dB and $|dB_{gsmz}|/\mathrm{B}_{magnitude}$, but also a low velocity $|V_{tot}|$ and $|V_{gsmx}|$ and a steep decrease in magnitude of the magnetic field can be observed. The previously mentioned peak in the proton density about one day before the HSS can now be identified with the steep increase in proton density shortly before the stream interface, while the density decreases rapidly after the stream interface, where subsequently the actual HSS is seen.

5.4 Alfvén waves

Most solar wind fluctuations are better seen in the magnetic field data because magnetic field experiments return samples at higher rate than plasma instruments such as SWEPAM. Many of these fluctuations in the solar wind are rather pure Alfvén waves propagating away from the Sun [1]. For low frequencies the magnetic field and velocity fluctuations of Alfvén waves are related as:

$$\delta\vec{v} = \pm\delta\vec{b}/\sqrt{\mu_0\rho} \tag{19}$$

where ρ is the mass density - in our case the proton density N multiplied by the proton mass $1.672622 \cdot 10^{-27}$ kg and where the fluctuations of the velocity and magnetic field components are the following

$$\delta\vec{v} = \text{Measured value from ACE} - \text{mean}(V_{gsmx}) \text{ over a two hour interval} \tag{20}$$

$$\delta\vec{b} = \text{Measured value from ACE} - \text{mean}(B_{gsmz}) \text{ over a two hour interval.} \tag{21}$$

Equ. 19 is an Alfvén wave solution of the MHD equations and is known as the Walen relation. The two-hour-average restriction used, is to assure that no average is taken over a time during which the velocity changes much. A positive correlation $\vec{v} - \vec{b}$ in Equ. 19 corresponds to a propagation of the waves antiparallel to the mean field (v_{plasma}-$v_{\text{Alfvén}}$) and a negative correlation corresponds to a parallel propagation [1].

5.5 Relation between the proton density N and the magnetic field fluctuations dB

Another crucial feature of HSS could be found by plotting the differential magnetic field (dB) against the proton number density (N), see Fig. 49 and Fig. 50. This provides new information about the relation between the velocity and the density of the plasma of HSSs. While during streams dB is small and nearly independent of N, during slow solar wind periods dB can be much higher whenever N is low. One may speculate that in a tenuous plasma particles have much more space to move. When the velocity is in the slow solar wind region, their path fluctuations can be much higher. This causes unsteadiness of the magnetic field, which is frozen into the plasma. During HSSs the path fluctuations are small due to high velocities and thus become nearly independent of the density. The plot also illustrate the higher densities of the slow solar wind.

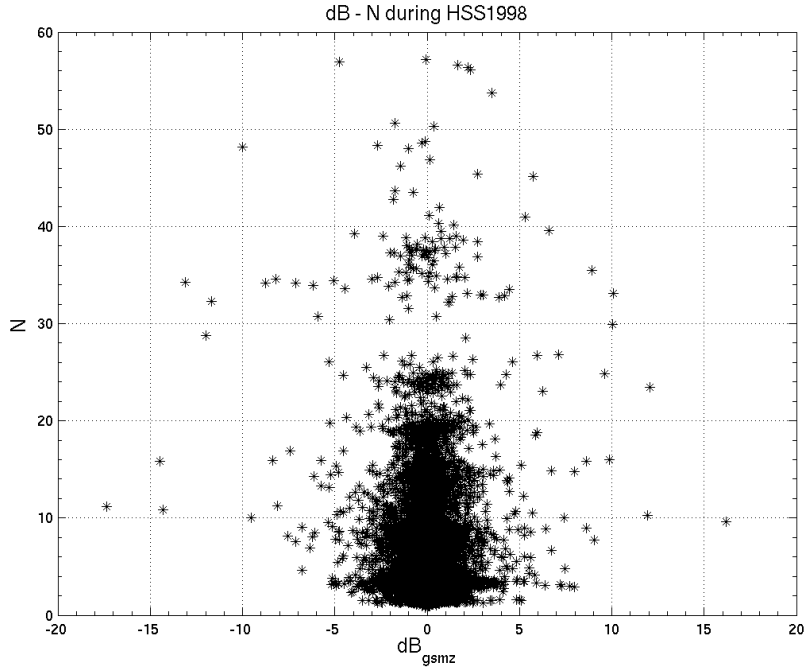

Fig. 49: dB versus N during HSS in 1998

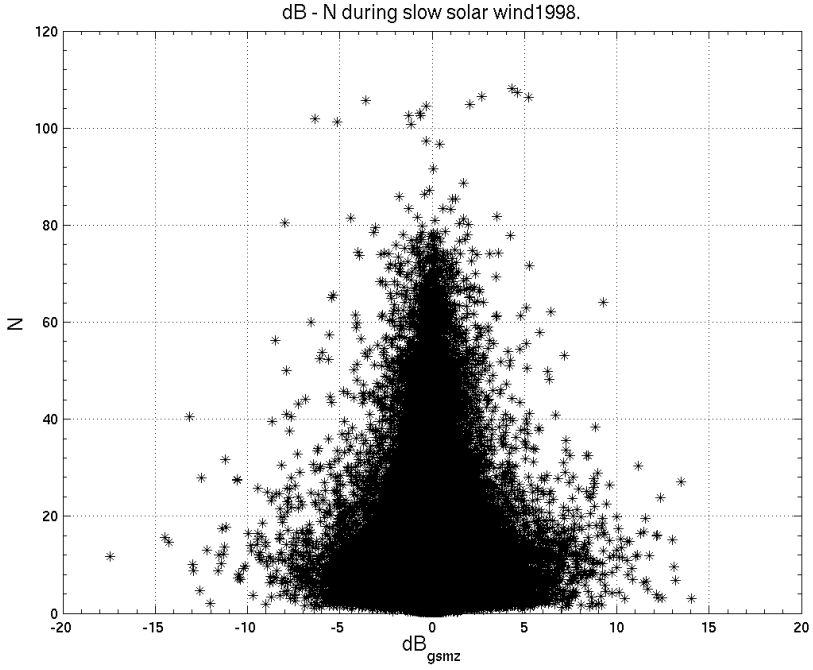

Fig. 50: dB versus N during slow solar wind periods in 1998

6 Separation of CMEs from HSSs

As summarised in Section 1.2.5 magnetic clouds are not related to HSSs. Their fraction from CMEs varies with the phase of the solar cycle, from ≅ 100% at solar minimum to ≅ 15% at solar maximum [15]. In May 1998 a magnetic cloud is found that is according to the two-level definition an HSS, but the curve features are clearly different from those of an HSS as can be seen in Fig. 51. The proton density is much higher than in average during HSSs. It also shows three broad peaks and no global slow decrease as the structure passes the spacecraft - unlike N during HSSs. The jumps in the B_{gsmz} component and the large-scale south- and northward turnings would also be exceptional for HSSs. Such structures need to be taken out of the HSS data set.

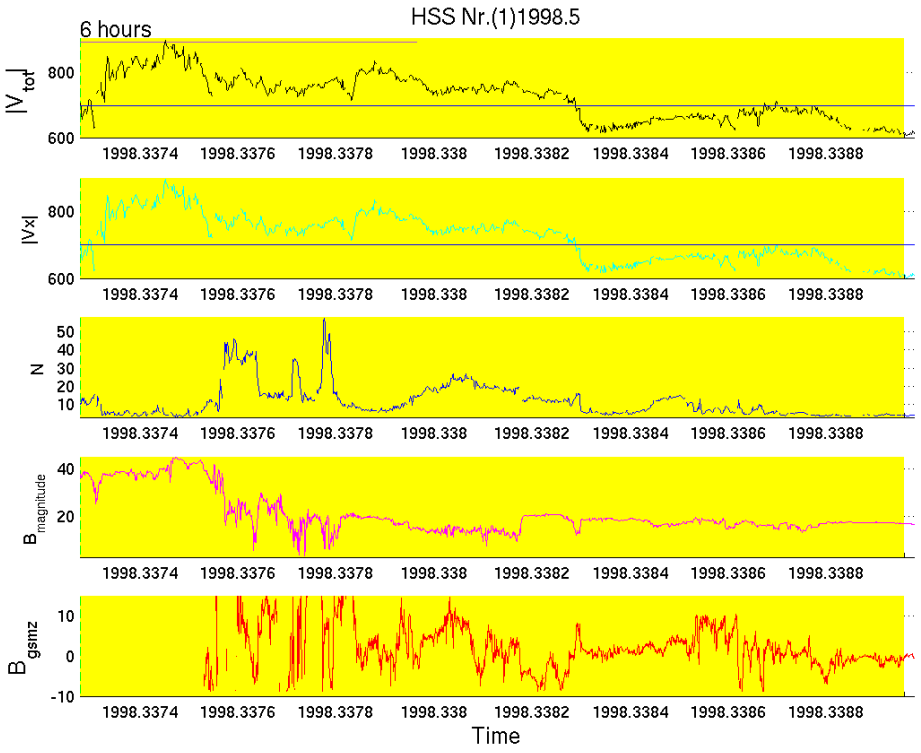

Fig. 51: Magnetic cloud (yellow background) on May 4 at 02:34:44 UT until 17:28:36 UT, 1998.

To extract the pure HSSs, one would need to substract from the data set the coronal mass ejections (CME), including also the magnetic clouds. One way would be to use a published list of coronal mass ejections. Another way to separate CMEs from HSSs is to make use of recent research results (e.g. Lee et al. [13]) which state that HSSs are accompanied by large amplitude Alfvén waves of the interplanetary magnetic field.

Most edges of HSSs are nonlinear, compressive large-amplitude magnetosonic waves (see Section 1.4), which have not yet steepend into a shock. The fast and slow solar wind streams are still relatively parallel to each other at a distance of 1 AU (see Fig. 52). At the beginning of HSSs at 1 AU are seldom (but possible) bow shocks or discontinuities. Shocks originating from CIRs occur mostly much further away from the Sun, where the fast and slow solar wind magnetic fields have larger angles with respect to each other.

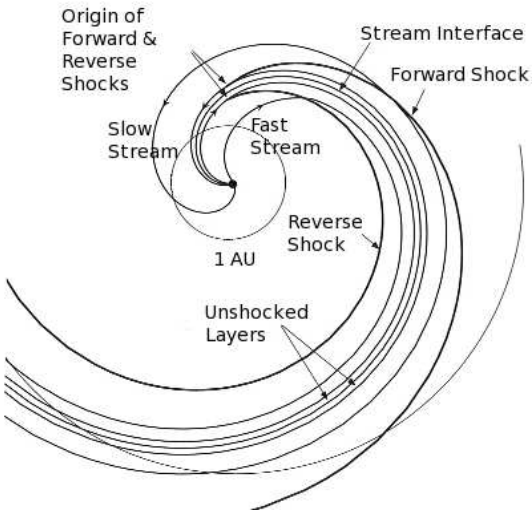

Fig. 52: Shock geometry in the frame of reference co-rotating with the Sun [1]

Initially the beginning of each HSS has to be examined for finding a typical shock structure: a fast and steep simultaneous increase in the solar wind parameters $|V_{gsmx}|$, B_{gsmz}, $B_{magnitude}$ and N. Since nearly all fast CMEs form shocks at 1 AU (slow CMEs are lower in velocity than 700 km/s and therefore need not to be considered), such shock structures in the HSS data set have to be analyzed more closely to make sure that they are HSSs rather than CMEs. A known characteristic of HSSs are the Alfvén waves that can be found at the beginning of an HSS, but not of a CME structure. The reason for this is the very compressive shock, with which the fast motion of CMEs starts from the Sun. It compresses the fluctuations and causes turbulences behind the shock, which are not associated with Alfvén waves. Fast streams, like HSSs, show directional fluctuations carried by the Alfvén waves and are usually incompressive. This criteria enables to distinguish between CMEs and HSSs.

To ascertain the presence of Alfvén waves by making use of Equ. 19, the following criteria have to be fulfilled:

- The fluctuations in the velocity component V_{gsmx} need to be small and approximately constant so that one can average over 2 h to calculate their mean value.
- The magnitude of the magnetic field ($B_{magnitude}$) must be about constant
- The magnetic field component B_{gsmz} should have a relatively constant magnitude

In Fig. 53 and Fig. 54 Equ. 19 is plotted. The green curve shows the fluctuations in the velocity V_{gsmz} and the blue curve $\pm\delta\vec{b}/\sqrt{\mu_0\rho}$. The unit of the y-axis is m/s. The lower panel in Fig. 53 clearly shows Alfvén waves in the first 10% of the total HSS duration on August 1 - 3 in 2003, propagating parallel to the mean field. On the other hand, Fig. 54 shows no Alfvén wave properties in the first 10% of the total HSS duration and thus seems to be rather a CME than an HSS.

It is interesting to notice that in the first 10% of HSS Alfvén waves are present. This may correlate with the observed and in the following section described high magnetic field fluctuations in the leading edge of HSSs. To make sure that the Alfvén waves can mainly be found in the first 10% of the HSS duration Equ. 19 was plotted for the entire HSS intervals. But surprisingly the Alfvén waves are as common in the rest of the HSS as in the first 10% of its duration. Thus strong magnetic fluctuations itself cannot be intrinsically assumed to be Alfvén waves. In several of the calculated data the median of the difference between $\delta\vec{v}$ and $\pm\delta\vec{b}/\sqrt{\mu_0\rho}$ was even higher for the first 10% of the duration of the HSS compared to the entire interval, meaning that the precision of the $\vec{v}-\vec{b}$ correlation can be even higher for the rest of the HSS interval.

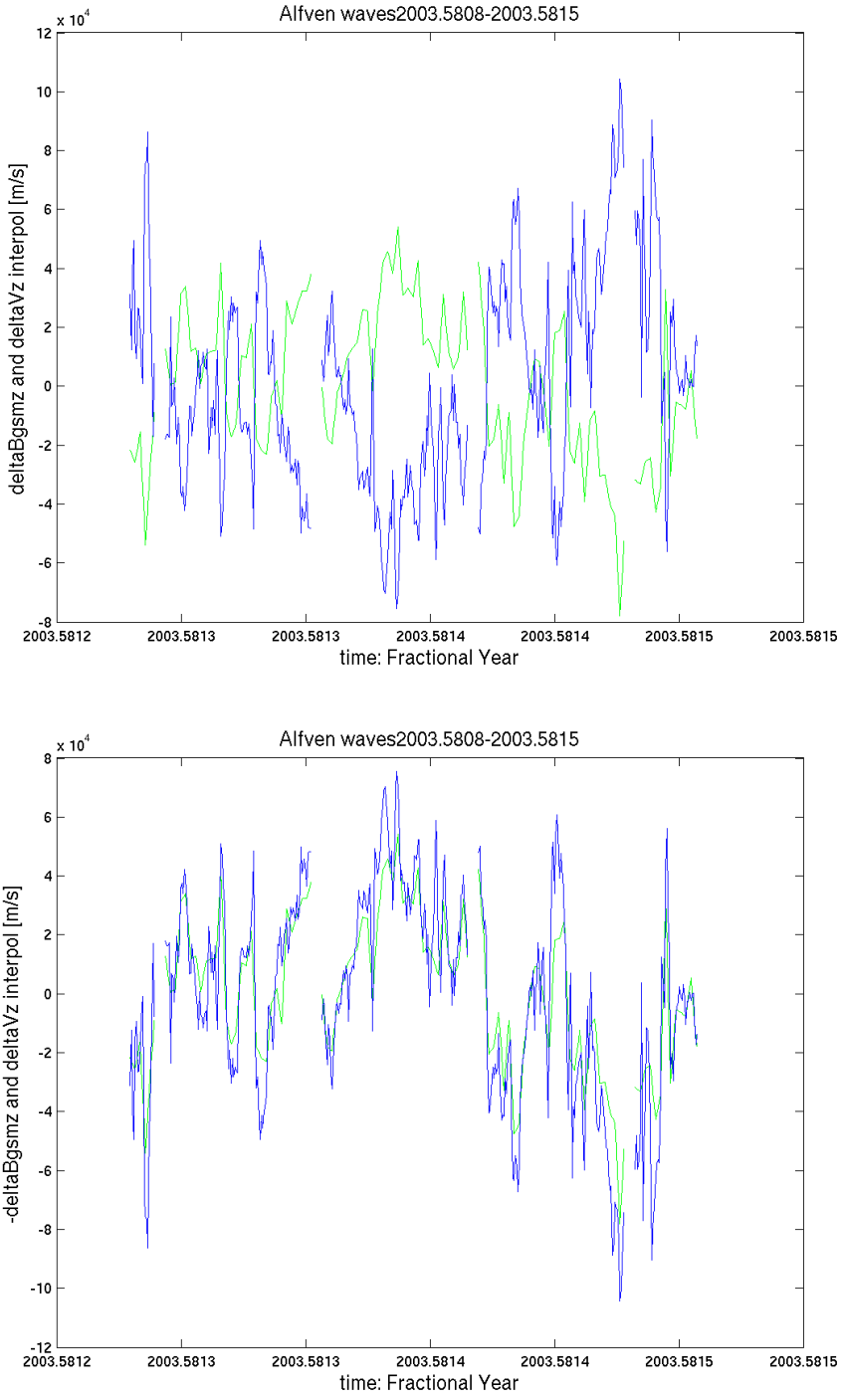

Fig. 53: Alfvén waves during the first 10% of the HSS on Aug 1 at 00:00:33 UT until Aug 3 at 12:38:08 UT, 2003. Plotted is Equ. 19.

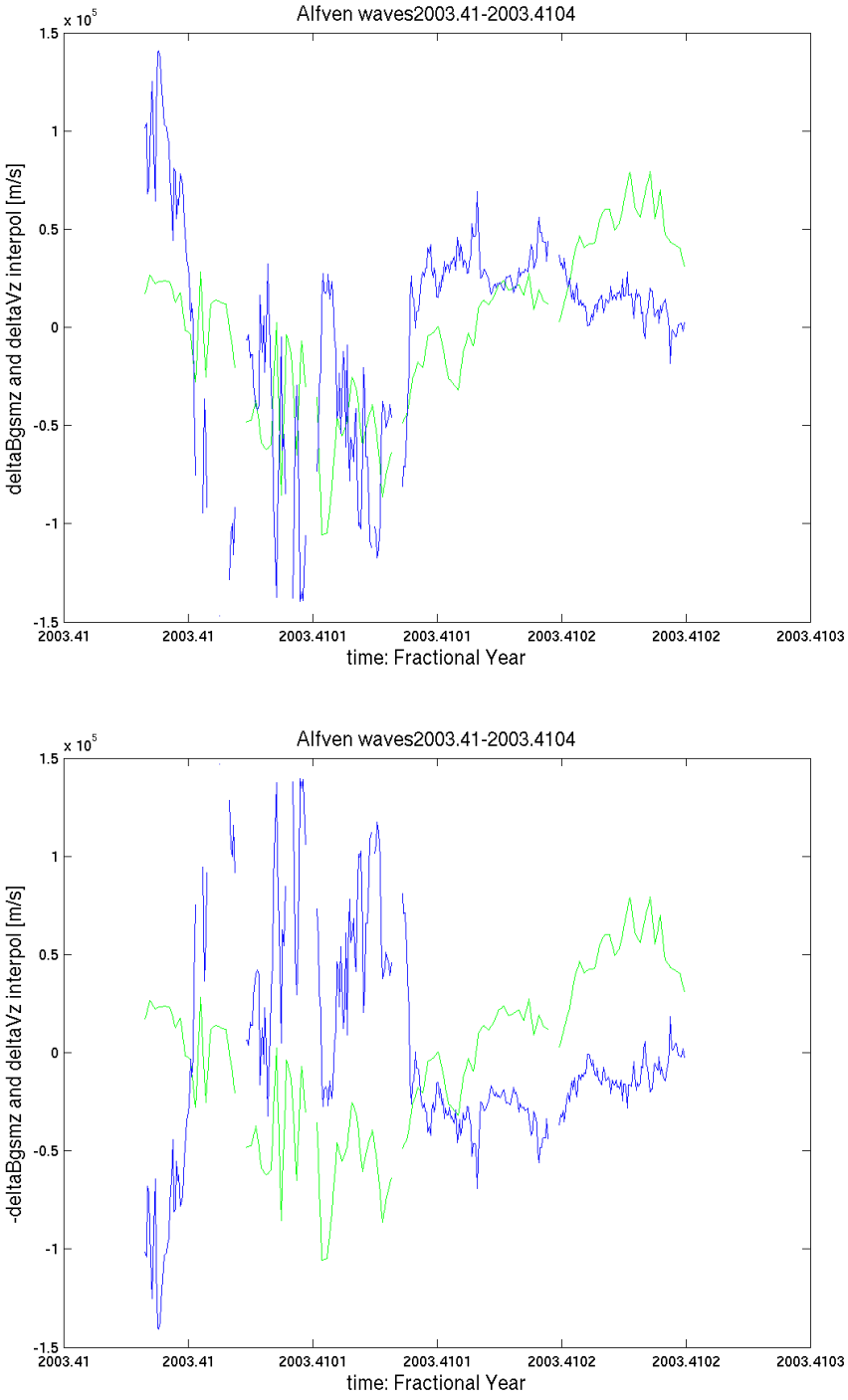

Fig. 54: No Alfvén wave properties during the first 10% of the HSS on May 30 at 15:53:13 UT until May 31 at 21:14:01 UT, 2003. Plotted is Equ. 19.

7 Discussion

As seen in the section about magnetic field fluctuation during HSS, the HSS definition has to be further improved to include all knowledge we have about their structure. The first step is to define at the beginning of an HSS the additional request of a fast velocity increase during a specified period of time. Therewith mistakes in the interpretation of graphics (Fig. 42 and Fig. 45) can be sorted out.

Some substorm times have been considered to see if they correspond to the beginning of the HSSs. To find out more about the substorm-HSS relation and to be able to make presumptions one would need to invest time into the substorm definition to produce a substorm list which must be carefully examined in order to find the percentage of cases where HSSs were triggering substorms. What was shown are similarities between substorms and HSSs regarding the AL indices.

The separation of HSS from CMEs by using the Alfvén wave requirement has to be evaluated by giving clear constraints, how much the two curves (see Fig. 19) can differ from each other in order to still be Alfvén waves. Further is planned to test the Walen relation equation for a typical CME event to see how much they differ from HSSs in the graphical illustration. Then the non HSSs are going to be substracted from the data set and compared how the plots differ from the previously received ones.

8 Conclusions

The task of this M.Sc. thesis was the examination of solar cycle variation of HSSs and their typical features represented by the solar wind parameters. In a first step HSS were defined according to their velocity distribution and then described with help of a superposed epoch analysis and two particular examples the decrease in the velocity and the proton density during an HSS and the correlation between the magnetic field and the proton density. Further the occurrence of HSSs and fast solar wind periods was illustrated during different phases of the solar cycle 23 and its dependence on the definition of HSSs was shown.

To gain a better understanding of the reason for the velocity and duration distribution of HSSs, the relation of the solar cycle to the coronal holes was studied by considering the years 1998 – 2006. The results are supported by scientific papers. Further the coronal hole evolution during a solar cycle was described and the correlation of occurrence of HSSs with the solar rotation was demonstrated.

An important step was then the conjunction of Alfvén waves, interplanetary magnetic field fluctuations and a low AL index during HSSs. The AL index was shown to be generally more negative during HSSs than during slow solar wind periods which raises the question of the correlation between HSSs and substorms, that is still not solved as well as the presumed correlation between HSSs and CIRs.

A remarkable result was found with the magnetic field fluctuations dB being small and independent of N during a stream, but not during slow solar wind periods.

Another important result is the higher z-component magnetic field and velocity fluctuations in the first 10 - 15% of an HSS period.

To distinguish between CMEs and HSSs the Walen relation and a magnetic cloud table were used. In addition the origin of the stream interface was discussed which was found to be in CIRs. At the end I started with the separation of the CMEs from the HSS data which still needs to be improved and brought to perfection.

9 Perspectives for the future

This research will be continued by further separating the high-speed streams from the coronal mass ejections to examine the various types of activity drivers separately.

To gain a better understanding of the interplanetary medium and its influence on the structure of HSSs, of interest would be to look at the origin of HSSs and their structure close to the Sun. By comparing these with the ACE data one could study the evolution of streams on their way to the Earth. The origin itself, the coronal holes, still hide their huge secret: How are HSS accelerated to 700 km/s? And how is the sunspot number related to coronal holes and correlate with the HSS structures?

The relationship between the coronal hole area and latitude to the different types of HSSs is an interesting topic to pursue. One of the open questions is the relationship between high-speed streams and co-rotating interaction regions (CIRs). Additionally some analysis should still be conducted to resolve the association of the HSSs with substorm activity. A specific question relates to solar wind features that are effective in substorm triggering.

10 Acknowledgments

I am very pleased that I was given the opportunity of working on the exciting and interesting topic of high-speed streams at the Finnish Meteorological Institute in Helsinki. It was a great way to start working on my future research field of space physics and I learnt a lot. I also realized at the end that there are much more open questions to find an answer to then I could reach during these eight months and this is what drives my motivation and curiosity that only can be pacified by further research.

First I would like to express my sincere thanks to my supervisors Assoc. Prof. Eija Tanskanen, Prof. Tuija Pulkkinen and Prof. Philippe Jetzer for their advice and support. Thanks go also to Dr. Walter Schmidt for his technical support and MSc. Liisa Juusola and Dr. Noora Partamies for the constructive discussions. I also express my gratitude to Prof. Tuija Pulkkinen and Prof. Hannu Koskinen for reading my thesis carefully and giving detailed feedback. To Dr. Rami Vainio I am grateful for his support with the Alfvén waves and their determination. And special thanks go to Mikko Kotiranta for helping whenever needed. I also thank the ACE SWEPAM and MAG instrument team and the ACE Science Center for providing the ACE data.

References

[1] A. Balogh, J. T. Gosling, J. R. Jokipii, R. Kallenbach, H. Kunow (Eds.); *Corotating Interaction Regions*, Kluwer Academic Publishers, Space Science Series of ISSI, vol.7, p.62-74 1999

[2] W. Baumjohann, R.A. Treumann; *Basic space plasma physics*, p.73-81, p.186-197, Imperial College Press, 1997

[3] J. W. Belcher, L. Davis, Jr.; *Large-amplitude Alfvén waves in the interplanetary medium*, Journal of geophysical research, 76, 3534, 1971

[4] L. F. Biermann; *Kometenschweife und solare Korpuskularstrahlung*, Zeitschrift für Astrophysik, vol. 29, p.274-286, 1951

[5] D. E. Billings, W. O. Roberts; *The origin of M-region geomagnetic storms*, Astrophysical Journal, vol. 130, 961, 1959

[6] L. F. Burlaga; *Interplanetary Magnetohydrodynamics*, Oxford University Press, 1995

[7] V. G. Fainshtein, G. V. Rudenko; *The birth of coronal holes*, Multi-wavelength investigations of solar activity proceedings 1 AU symposium No. 223, 2004

[8] A. J. Hundhausen; *Coronal expansion and solar wind*, Springer-Verlag, 1972

[9] M. G. Kivelson, Ch.T. Russell; *Introduction to space physics*, p.58-88 and p.91-129, Cambridge University Press, 1995

[10] A. S. Krieger, A. F. Timothy, E. C. Roelof; *A coronal hole and its identification as the source of a high velocity solar wind stream*, Solar Physics, vol. 29, 5005, 1973

[11] K. R. Lang; *The Cambridge Encyclopedia of the Sun*, p.148-182, Cambridge University Press, 2001

[12] R. Lanza, A. Meloni; *The Earth's Magnetism*, Springer, 2006

[13] D.-Y. Lee, L.R. Lyons, K.C. Kim, J.-H. Baek, K.-H.Kim, J.Weygand, Y.-J. Moon, K.-S. Cho, Y. D. Park, W. Han; *Repetitive substorms caused by Alfvénic waves of the interplanetary magnetic field during high-speed solar wind streams*, Journal of geophysical research, vol. 111, A12214, 2006

[14] R. P. Lepping, J. A. Jones, L. F. Burlaga; *Magnetic field structure of interplanetary magnetic clouds at 1 AU*, Journal of geophysical research, 95, 11, 957, 1990

[15] I. G. Richardson, H.V. Cane; *The fraction of interplanetary coronal mass ejections that are magnetic clouds: Evidence for a solar cycle variation*, Geophysical Research Letters, vol. 31, Issue 18, 09/2004

[16] S. Robbins, C. J. Henney, J. W. Harvey; *Solar wind forecasting with coronal holes*, Kluwer Academic Publishers, 11/2005

[17] E. N. Parker; *Dynamics of the interplanetary gas and magnetic fields*, Astrophysical Journal, vol. 128, 664, 1958

[18] E. N. Parker; *Interplanetary dynamical processes*, Wiley-Interscience, New York, 1963

[19] E. I. Tanskanen; *Terrestrial substorms as a part of global energy flow*, Academic Dissertation, 03/2002

[20] E. I. Tanskanen; *Magnetospheric substorms are strongly modulated by interplanetary high-speed streams*, Geophysical Research Letters, vol. 32, Issue 16, 08/2005

[21] Lecture notes of R. Vainio; *Shock waves and energetic particles in space plasmas*, University of Helsinki, 2006

[22] Lecture notes of R. Vainio; *Solar Physics*, University of Helsinki, 2005

[23] Jun Zhang, J. Woch, S. Solanki; *Polar coronal holes during solar cycle 22 and 23*, Astronomy&Astrophysics, vol. 5, No. 5, p.531-538, 2005

[24] I. Cairns; *Co-rotating Interaction Regions: interactions between fast and slow streams*, 09/01/1999,
http://www.physics.usyd.edu.au/∼cairns/teaching/lecture11/node4.html

[25] E. R. Christian, 12/18/2003,
http://helios.gsfc.nasa.gov/ace/gallery.html

[26] D. O'Donoghue, *First Science with SALT: Observations of Eclipsing Polar*, 11/21/2006,
http://www.science.psu.edu/alert/Ramsey8-2006.htm

[27] Ch. W. Smith; *ACE/MAG Project MAG Instrument*, 08/29/2003,
http://www.ssg.sr.unh.edu/mag/ace/instrument.html

[28] Data Analysis Center for Geomagnetism and Space Magnetism Graduate School of Science (No author), 04/10/2007,
http://swdcwww.kugi.kyoto-u.ac.jp/aedir/

[29] The Ohio State University (No author), 11/2007,
http://www.astronomy.ohio-state.edu/frogel/Ast161/outline161_a00_part13.html

[30] University of Bergen (No author), 11/2007,
http://web.ift.uib.no/Romfysikk/RESEARCH/PROJECTS/CLUSTER/

[31] University of Leicester (No author), 03/03/1997,
http://ion.le.ac.uk/images/magnetosphere/substorm.gif

[32] University of Melbourne (No author), *Introduction to geophysical exploration*, 07/24/2000,
http://www.earthsci.unimelb.edu.au/ES304/MODULES/MAG/NOTES/

[33] National Oceanic and Atmospheric Administration (NOAA) (No author), *Next solar storm cycle will start late*, 04/25/2007,
http://www.swpc.noaa.gov/SolarCycle/SC24/PressRelease.html

[34] (No author), *SWEPAM*, 06/26/2006,
http://swepam.lanl.gov/